The Influence of Composition and Plastic Strain on the Electrochemistry of Stainless Steels Doped with Platinum Group Metals

K. Govender, O. Necib, I. I. Ahmed, F Scenini,
S. Lyon and A. H. Sherry
The University of Manchester

D. Saxey, A. Cerezo, A. Wilkinson,
C. Grovenor and G. Smith
Oxford University

B. Connolly and C. Cooper
University of Birmingham

E. Rowsell, A. Fones, and A. Pratt
Johnson Matthey

Date:	March 2009
Report Number:	MPC/R/076
Issue Number	1

Title	The Influence of Composition and Plastic Strain on the Electrochemistry of Stainless Steels Doped with Platinum Group Metals
Authors	K. Govender, O. Necib, I. Ahmed, F Scenini, S. Lyon and A.H. Sherry (The University of Manchester) D. Saxey, A. Cerezo, A. Wilkinson, C Grovenor and G. Smith (Oxford University) B Connolly and C Cooper (Birmingham University) E. Rowsell, A. Fones, and A. Pratt (Johnson Matthey)
Customer	MoD
Customer reference	R&T/1/0231
Our reference	R012849/RCP1045
Deliverable	D7
Report number	MPC/R/076
Report status	Issue 1
Corresponding author	Prof. A H Sherry Materials Performance Centre School of Materials University of Manchester Sackville Street Manchester M60 1QD Tel: 0161 306 4842 Fax: 0161 306 4865 E-mail:andrew.sherry@manchester.ac.uk

Executive Summary

Corrosion-related degradation of stainless steel components of Naval Nuclear Power Plant (NNPP) can have significant impact on the cost of nuclear ownership through inspection requirements, the reliability and, in some cases, the availability of plant. This project aims to establish an improved physical understanding of the mechanisms of Stress Corrosion Cracking (SCC) of 304 stainless steel of the type used for a range of NNPP components. In order to accomplish this aim, the research is studying the influence of platinum group metal (PGM) alloying additions (i.e. < 1 wt.%, additions palladium and/or ruthenium) on the SCC of 304 stainless steel as these have predictable effects on the electrochemical processes of corrosion. The approach includes mechanical and electrochemical testing together with pre- and post-test metallurgical examination (over an appropriate range of length scales), and finally predictive model development. This Report presents experimental data relating to the influence of PGM additions and plastic-strain (cold work) on the electrochemistry of 304L stainless steel in a range of environments including simulated PWR water.

The electrochemical data reveal ruthenium to be more effective than palladium in enhancing the corrosion resistance of 304 stainless steel in PWR water chemistry and this was traced to removal of palladium from the alloy matrix by precipitation of a PdMn Intermetallic 2nd phase precipitate (reported previously). For all alloy variants, increasing temperature shifted the Open Circuit Potential (OCP) to more noble values and increased the anodic current density; observations consistent with enhanced to both metal dissolution and oxygen diffusion rates at higher temperatures. Increasing the oxygen concentration increased the OCP but decreased the passive current density; observations rationalised in terms of the efficiency of the cathodic reaction in which PGM additions enhance the exchange current density for oxygen reduction leading to faster passivation kinetics. In hydrogenated water, the PGM modified alloys displayed a preferred lower OCP and a higher anodic current density than the standard alloy and this is because PGM additions increase the exchange current density for hydrogen oxidation. In deaerated pressurised water at 260°C, the ruthenium-doped alloy displayed an improved corrosion resistance compared with standard 304 stainless steel whilst the palladium-doped alloy displayed a higher dissolution current density. Studies in acidified aerated potassium tetrathionate revealed an abrupt transition of the OCP to more positive potentials the effect being more rapid for the ruthenium-doped alloy. Analysis of the anodic polarisation

curves suggests that PGM additions enhance the corrosion resistance, the effect being most pronounced for ruthenium.

Regarding the effect of plastic strain (cold work), the influence of strain path on the evolution of internal strain in cold-worked austenitic stainless steel was investigated using neutron diffraction and mechanical testing. As expected, hardness and yield strength increase with the level of cold work, however the magnitude of the increase is dependent upon the strain path due to the mixed isotropic/kinematic hardening response. Neutron diffraction demonstrated that residual strain in cold-worked material increases with the level of cold work. The elastic anisotropy and the lattice strain difference increased consistently with the applied stress during *in-situ* re-straining tests. In considering all the cold work material reloaded *in-situ* to 5 % in tension along the 3 principal directions, the largest strain was found to occur in the material with the pre-strain level of 20 % reduction. Electrochemical data indicate that the sample orientation (and, consequently the alloy texture) has a greater effect than the absolute level of cold work. Thus, the L-T plane displayed more noble electrochemical behaviour than the L-S plane, and the T-S plane was found to be least noble. Generally, material cold rolled to 20% reduction showed the least noble electrochemical behaviour of all the cold rolled materials on all three orthogonal planes.

Contents

1 INTRODUCTION 6

2 EXPERIMENTAL 8

2.1 Part A – Electrochemistry in acidified tetrathionate solutions and simulated PWR environments 8
2.1.1 Materials and heat-treatment 8
2.1.2 Low-temperature electrochemical studies 8
2.1.3 High-temperature electrochemical studies 9

2.2 Part B – Electrochemical and mechanical studies of cold worked 304L SS 10
2.2.1 Materials and processing 10
2.2.2 Electrochemical studies 12
2.2.3 Mechanical studies 12

3 RESULTS 15

3.1 Part A – Electrochemistry in acidified tetrathionate and simulated PWR environments 15
3.1.1 Electrochemical measurements in PWR water 15
3.1.2 Electrochemical measurements in acidified tetrathionate solutions 28

3.2 Part B – Electrochemical and mechanical studies of cold worked 304L SS 34
3.2.1 Electrochemical studies of CW 304L SS 34
(a) Longitudinal Direction 38
(b) Transverse Direction 39
(c) Short-Transverse Direction 39
3.2.3 Mechanical studies of cold worked 304L SS 41
(a) Annealed 42
(b) 5 % Cold Work 42
(c) 10% Cold Work 43
(d) 20 % Cold Work 43
(e) 40% Cold Work 44

4. DISCUSSION 56

4.1 Part A – Electrochemistry in acidified tetrathionate and simulated PWR environments 56
4.1.1 Electrochemical measurements in PWR water 56
4.1.2. Electrochemical studies in acidified tetrathionate solutions 58

4.2 Part B – Electrochemical and mechanical studies of cold worked 304L SS 59
4.2.1 Electrochemical studies of CW 304 SS 59
4.2.2 Mechanical studies of 304L SS 60

5. CONCLUDING REMARKS 62

6. REFERENCES 64

1 Introduction

Corrosion-related degradation of stainless steel components of Naval Nuclear Power Plant (NNPP) have significant impacts on the cost of nuclear ownership through inspection requirements, the reliability of components and, importantly, on plant availability. This research aims to establish an improved physical understanding of the mechanisms of Stress Corrosion Cracking (SCC) of 304L stainless steel of the type used for a range of NNPP components by use of small < 1% of palladium and/or ruthenium additions. The approach includes mechanical and electrochemical testing alongside pre- and post-test metallurgical examination over a range of scale-lengths, and importantly, predictive model development. This Report includes results from two investigations, which form part of the overall project:

- Part A addresses the electrochemical behaviour of virgin and PGM-modified stainless steels in both acidified tetrathionate solutions and simulated PWR environments.
- Part B addresses the influence of plastic strain generated through cold work on SCC in austenitic stainless steels. The latter section incorporates results from both electrochemical and mechanical studies of cold worked 304L stainless steels.

The objective of the electrochemical studies in PWR water was to compare the corrosion characteristics of the PGM-modified 304SS with the standard alloy, acquiring data for input into models for corrosion-related degradation under reactor conditions. The second electrolyte, acidified potassium tetrathionate, provided a model environment for further electrochemical studies as this medium facilitates intergranular corrosion (IGC) and intergranular stress corrosion cracking (IGSCC) in sensitised stainless steels.

Part B of the report presents research undertaken to address the influence of cold work on SCC susceptibility of 304L stainless steels. Cold working of materials is often carried out to improve the mechanical properties and the surface finish of the material and is also an inevitable consequence of metal forming operations. Cold work causes significant changes to the geometry and orientation of the grains with respect to the deformation direction. Similarly, the degree of cold reduction and strain heterogeneity that exist in materials subjected to cold work may also cause electrochemical potential differences across the material. Grain boundaries, having been identified as the regions of higher energy, are generally relatively more active than the grain matrix [1]. The objective of the first set of experiments was to assess how

cold work and anisotropy influence the electrochemical behaviour of 304L stainless steels in a corrosive environment. Open circuit potential (OCP) and anodic potentiodynamic polarisation measurements were carried out on solution-annealed 304L subjected to different levels of cold work.

Individual grains within a single phase polycrystalline material subjected to plastic deformation will have a strain response that is dependent their orientation with the loading axis. Thus, the slip systems of grains that have favourable orientations to the loading axis will activate at an earlier stage in the deformation process. The elastic strain that develops in non-aligned grains helps to accommodate the inhomogeneous and non-reversible plastic deformation in the adjacent grains during the elasto-plastic transition. The resultant elastic strains present after complete removal of the load are considered as residual strain. Type II strains are intergranular residual strains which are averaged over several grains scale along a particular crystallographic direction [2, 3]. It is recognised that a great deal of work has been done on the prediction of internal elastic strain following uniaxial loading under plane strain with Elasto-Plastic Self Consistent (EPSC) modelling [2, 4]. However, Crystal Plastic Finite Element Modelling (CPFEM) offers a more comprehensive approach purposely developed to explore the mechanical aspects of the cold work effects on the SCC. The model has been used to assess the influence of the various degrees of cold rolling (pre-strain) and re-strain along the 3 principal directions on the development of internal stress and strain at the micro-scale level [5].

Against this background, the second objective of Part B was to assess how cold work affects the mechanical driving force for SCC in austenitic stainless steels including the yield strength, hardness values and internal strain evolution at grain scale when loaded along each of the three principal directions. Neutron diffraction was used for the measurement of the lattice elastic strain in cold rolled materials *ex-situ* and also during the *in-situ* loading to 5 % plastic strain along the three principal directions. Experimental data, required for the validation of the CPFM model, were generated.

2 Experimental

2.1 Part A – Electrochemistry in acidified tetrathionate solutions and simulated PWR environments

2.1.1 Materials and heat-treatment

All alloys used in this study were vacuum-melted and the cast ingots surface ground (to remove surface segregants) before cutting for plate production. Cut pieces were hot-rolled, then cold rolled to approximately a 30% reduction of area and solution-annealed for 40 min at 1050°C followed by an air cool. The chemical composition of the alloys used in Part A is given in Table 1. Sensitisation, when required, was carried out by heating in an argon atmosphere to 650°C for 24 h.

Table 1 Chemical composition of the alloys (wt%) used in Part A.

	Si	Cr	Mn	Fe	Ni	C	S	Pd	Ru	Co	Cu	Mo	V	P
304 MC	0.74	19.01	1.52	68.64	9.4	0.056	0.006			<0.05	0.44	0.26	<0.05	0.006
Pd3MC	0.60	18.29	1.80	67.53	9.39	0.050	0.020	0.96	<0.01	0.10	0.58	0.30	0.08	0.03
Ru1MC	0.57	18.68	1.55	67.49	9.54	0.041	0.001	-	0.13	-	0.51	0.33	0.10	0.02
Ru2MC	0.51	18.88	1.97	67.98	9.57	0.035	0.001	-	0.26	-	0.51	0.31	0.09	0.024
Ru3MC	0.53	18.39	1.67	68.32	9.41	0.047	0.022	<0.01	1.01	0.11	0.54	0.32	0.07	0.029

2.1.2 Low-temperature electrochemical studies

Electrochemical experiments were conducted in a three-electrode cell consisting of the specimen (or working electrode), a platinum counter electrode and a saturated calomel reference electrode (SCE) and employing a Solartron Model 1286 potentiostat and CorrWare software as experimental equipment. The reference electrode was connected to the cell using a remote gel bridge with a capillary probe placed very close to the sample in order to reduce the cell resistance. Open circuit potential (OCP) measurements and potentiodynamic scans were carried out in two electrolytes: (a) solution containing 1000 ppm B + 2 ppm Li (as boric acid and lithium hydroxide), pH~7; and (b) 0.01 M $K_2S_4O_6$ solution (acidified to pH 1.5 with H_2SO_4). In the first electrolye, the measurements were carried out under aerated, deaerated (by nitrogen purging) or hydrogenated conditions with a scan rate of 1 mV s^{-1} whilst for the second electrolyte (acidified tetrathionate), scan rates of 0.5 and 5 mV s^{-1} were used. Electrical

connection outside the cell was made by connecting the specimens to copper wire by spot welding; this was isolated from the electrolyte solution by heat-shrink polyolefin wrapping and by embedding the sample plus wire in epoxy resin. The exposed surfaces, 1 cm^2 in area, were polished to 1200 grade SiC finish, and cleaned with distilled water and acetone before the start of each electrochemical experiment. The interface between the sample edges and the mounting material was masked using a commercial lacquer (Lacomite) to limit the initiation of crevice corrosion. The tests performed in the first electrolyte were done over a range of temperatures (indicated below) whilst experiments in the tetrathionate were carried out at laboratory ambient temperature (25°C). All temperatures were controlled by immersion of the electrochemical call in a water bath (Grant GD 100). Prior to the initiation of the polarisation scans, the samples were immersed in the electrolytes for 30 minutes to obtain a stable OCP. In order to demonstrate reproducibility, all the experiments were repeated at least three times.

2.1.3 High-temperature electrochemical studies

This set of electrochemical experiments were run in a 10kN slow strain rate tensile (SSRT) static autoclave (Cormet testing systems), made of alloy C-276. The maximum operating temperature was 350°C and the maximum operating pressure was 220 bar. For the high temperature tests, alloys 304MC, Pd3MC (1 wt. % Pd), Ru3MC (1 wt. % Ru) were used with all alloys in the sensitised condition. The 1 cm^3 samples were ground down to a 1200 SiC surface finish on all the faces. They were subsequently cleaned with deionised water and acetone prior to being spot-welded to a nichrome wire. All faces of the sample were exposed to solution during the electrochemical measurements. The operating temperature was 260°C, and a temperature ramp rate of 100K/hour was used to increase the temperature up to the required value; only once this had been achieved were the experiments started. The corresponding pressure was 48 bar at 260°C, respectively. The solution used was the same one used in the above-mentioned experiments (1000 ppm B + 2 ppm Li, pH~7 at RT). This was either deaerated (by nitrogen purging for 40 minutes) or hydrogenated at 30ml hydrogen per litre of water (by initial dearation followed by introduction of hydrogen). The electrochemical measurements were conducted using Cormet softwaree running" at a scan rate of 1 mV s^{-1}. A reference electrode (Pd coupled with Pt wire), manufactured by Cormet Testing Systems, and a Pt counter electrode were used in the setup. The reference electrode was re-calibrated at each temperature prior to the start of the experiments.

For these tests, the OCP was measured until it was stable and then a potentiodynamic scan was initiated from -0.3 below the OCP to +1.5V above the OCP. The same sample was used for a whole set of experiments.

2.2 Part B – Electrochemical and mechanical studies of cold worked 304L SS

2.2.1 Materials and processing

The material used for experiments in Part B was type 304L austenitic stainless steel with the chemical composition given in Table 2. The as-received material was solution-annealed at 1050°C for 30 min and water quenched. The annealed material was subsequently cold worked by multipass rolling leading to 5%, 10%, 20% and 40% reductions in the through thickness.

Table 2: Measured chemical composition of 304L used in experiments in Part B

	C	Cr	Mn	N	Ni	P	S	Si
304L	0.030	18.387	1.804	0.086	8.133	0.034	0.005	0.411

For the electrochemical studies, the tested specimens were obtained in 5 different processing conditions, which corresponded to 4 in the cold rolled condition (i.e. 5%, 10%, 20% and 40% reduction in thickness) and one in the annealed state. Samples were obtained from the three orthogonal planes in each of the material conditions (Figure 1). The three colour coded planes namely: S-T (purple), S-L (red) and L-T (blue) planes are perpendicular to the Longitudinal (L), Transverse (T) and Short-transverse (S) directions respectively. However, the naming convention used for the samples in the report includes *e.g.* AN-L, 5% CW-T. The first part of the name before the hyphen represents the material treatment conditions which include: Annealed, 5% CW, 10% CW, 20% CW and 40% CW and the second part after the hyphen indicate the *normal* direction to the sample surface namely L, T and S.

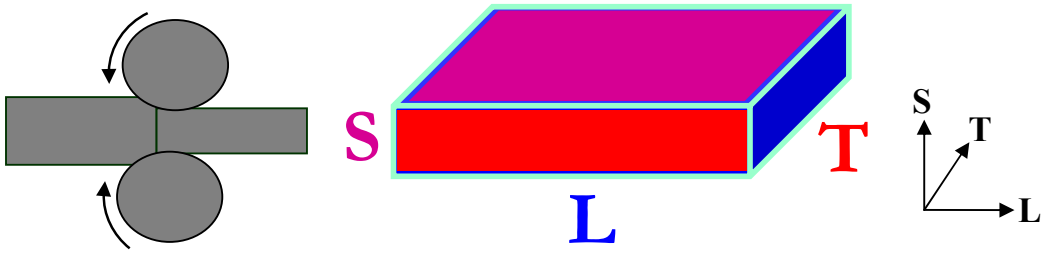

Figure 1 Schematic diagram of cold -rolled plate

The samples used for stress-strain tests and neutron diffraction experiments were machined along the three principal directions namely: Longitudinal (L), Transverse (T) and Short-transverse (S) directions in each of the material conditions (Figure 2). The material along the S-direction was too short to obtain a tensile specimen; it was therefore electron beam welded on both sides with Super Duplex Stainless Steel (SDSS) material, UNS S32760 (Figure 2). The choice of SDSS with relatively higher yield strength was made to allow load transfer to the austenitic stainless steel in the gauge length region. The tensile specimen was then machined from the assembly. Vickers hardness measurements were carried out on the different sample planes *viz.*: S-T, S-L and L-T planes which are perpendicular to the L, T and S directions, respectively.

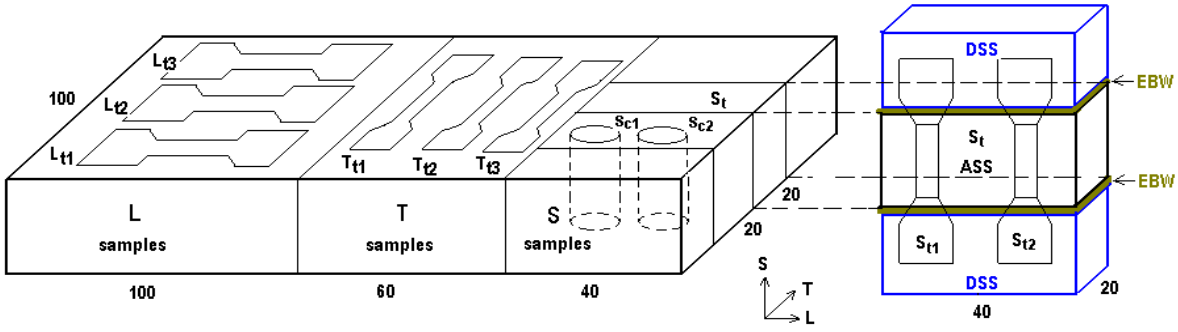

Figure 2 Schematic diagram of the cold rolled plate showing the specimen orientations

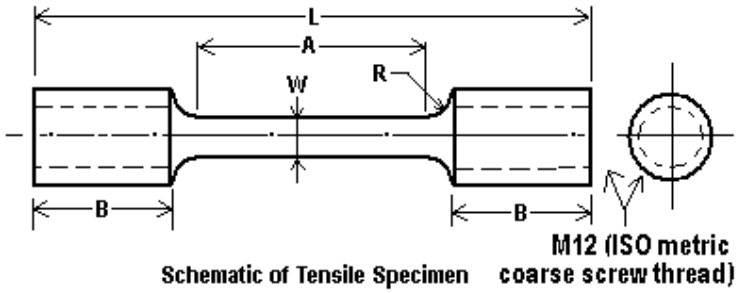

Schematic of Tensile Specimen

	Dimensions (mm)	
	Tensile	**Compressive**
A	26	14
B	20	28
L	82	74
R	8	2
W	8	8

Figure 3: Schematic diagram of the neutron diffraction (Engin-X) tension/compression specimen

The schematic diagram of the tension/compression samples and their respective dimensions are shown in Figure 3. Tension and compression specimens were both used for mechanical testing and neutron diffraction experiments.

2.2.2 Electrochemical studies

Cold worked samples for electrochemical testing were prepared as described in 2.1.2 above except that the final metallographic grinding was carried out to a 4000 grit finish. The electrochemical cell was set up following the procedures in the ASTM Standards G5-94 [6]. The electrolyte used for these experiments was 2M sulphuric acid (H_2SO_4), maintained at a temperature of 30°C for the duration of the experiment. The solution was deaerated using nitrogen gas bubbling for 30 minutes before the test. The OCP was recorded over a timescale of 3300 s; subsequently, anodic potentiodynamic polarisation (APP) measurement was carried out at the scan rate of 1mV s^{-1} over the potential range of -0.5 V to 0.25 V *vs.* SCE. The software used for data acquisition and analysis were CorrWare and CorrView respectively.

2.2.3 Mechanical studies

2.2.3.1 Hardness measurements

Sample preparation was carried out following the basic metallographic wet grinding with silicon carbide paper in grit order of 320, 400, 600, 800, 1200 and 4000. They were subsequently polished with diamond paste in order of 3 μm to 1 μm. A 30 kg load was used to

produce diamond-shaped indentations on the specimen surface from which the Vickers hardness values were calculated. The hardness profile along the 3 principal directions was investigated by carefully monitoring the size and direction of the 2 diagonals of the indentation on sample surfaces. Measurement was carried out along two parallel lines adequately separated to minimise the effect of localised plastic strain, on the 2 perpendicular planes of the specimen. Approximately 1 mm intervals between the indentations along each line were allowed during the measurements.

2.2.3.2 Mechanical testing

The stress-strain measurement was carried out on a 100 kN, Alliance-RT/100 tensile testing equipment. The specimen design and dimensions are shown in Figure 3. The test speed and the frequency of the data acquisition were 0.5 mm/minute and 10 Hz respectively. The load reversal test was carried out on the annealed materials, during which the specimens were initially loaded to 10 % strain both in tension and compression, then unloaded and subsequently reloaded to 5 % strain in tension. The cold worked specimens obtained from the 3 principal directions were loaded to 5 % strain and then unloaded to investigate the effect of pre-strain on the strain path.

2.2.3.3 Neutron diffraction experiments

2.2.3.3.1 Residual Strain Measurement

Residual and lattice strain measurements were carried out on the Engin-X diffractometer at ISIS, Rutherford Appleton Laboratory (RAL), Oxford; this is a time-of-flight neutron diffractometer with two banks of detectors positioned at ±90º to the incident beam (Figure 4). The banks define two measurement directions: Q_N and Q_S, along the specimen axis and perpendicular to the specimen axis respectively. The specimen (Figure 3) was mounted on the holder and then screwed on to the stage; the effective gauge volume was about 0.1 cm^3 (4 x 6 x 4 mm^3).

The residual strains in the rolled plate were measured by rotating the angle the sample makes with incoming beam, ω through: -15º, -30º, -45º, -60º and -75º. In a conventional $\sin^2\psi$ setup, this corresponds to ψ angles between 60º to 120º and -30º to 30º for the strain data along the specimen axis and perpendicular to the specimen axis respectively (Figure 4B). Data acquisition and analysis was carried out using the Open Genie software for the single peaks

fitting to determine the variation in d-spacing with direction. The residual strain data were plotted against the $\sin^2\psi$.

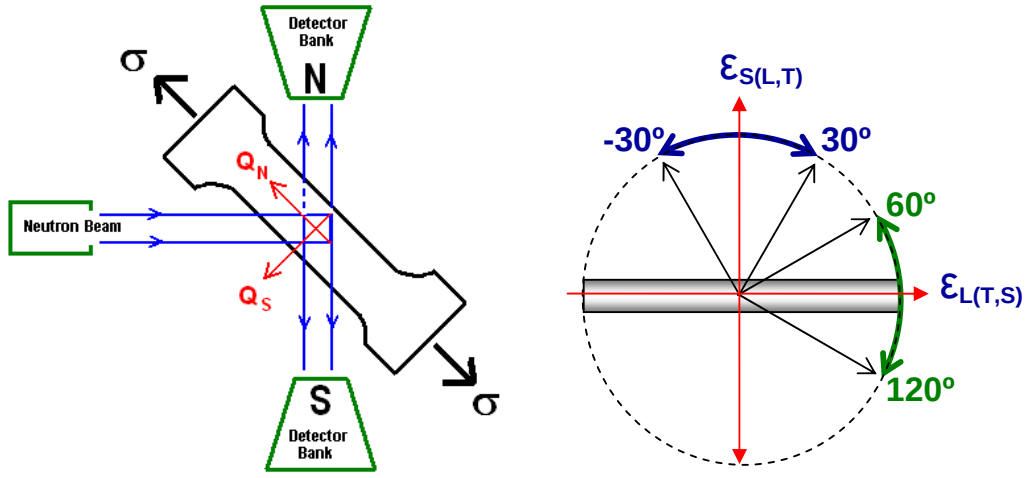

(A) (B)

Figure 4: Specimen orientation on the ISIS Engin-X neutron beam for the strain measurement parallel, Q_N and perpendicular, Q_S to the loading axis (A), and crystal orientations at which strains were measured on sample L-S (B)

2.2.3.3.2 In-Situ Loading Strain Measurement

The *in-situ* loading test was also carried out on the Engin-X neutron beam line. A horizontal stress rig used was mounted on the positioning table on the beam line. On average, 25 measurements were made on each sample during *in-situ* loading to 5 % tensile strain on the stress rig. The experiments were carried out predominantly under strain control except for the compression-tension loading specimen, which was under stress control during load reversal. All the neutron diffraction experiments were carried out at room temperature.

3 Results

3.1 Part A – Electrochemistry in acidified tetrathionate and simulated PWR environments

3.1.1 Electrochemical measurements in PWR water

3.1.1.1 Low temperature electrochemical tests

For each experiment, the open circuit potential was measured against a saturated calomel electrode (SCE) for 30 min in order to obtain a steady OCP. For measurements carried out under aerated conditions at 25°C, the OCP for the standard 304SS and the Pd- and Ru-modified 304SS were compared to the value for pure Pt metal and are shown in Figure 5(a). The Pt electrode has a positive OCP (+0.05 V_{SCE}) and the most noble potential. Whilst Ru additions cause a positive shift in the OCP (~ + 0.015V) compared to the standard 304SS, the OCP of the Pd alloy appears to be lower than the base alloy (~ – 0.05V).

For experiments carried out under similar chemical conditions but at 70°C, OCP *vs*. time is shown in Figure 5(b). In contrast to the results obtained at 2°C, the OCP values follow the trend in terms of nobility Pt>>Ru3MC>Pd3MC>304MC. No significant change was observed in the OCP over the 30 min period, with the exception of measurements recorded under aerated conditions at 70°C , where there was a slight decrease of the OCP with time (from +0.32V_{SCE} to +0.29 V_{SCE}) for Pt and an increase from -0.3 V_{SCE} to -0.2 V_{SCE} for 304MC. An increase in temperature appears to result in a shift in OCP to more noble values for the PGM-modified alloys and pure Pt, but gave rise to a less noble value for the 304SS. Under deaerated conditions (by nitrogen purging), at both 25 °C and 70°C, OCP values follow the same order as for aerated conditions at 70°C, *i.e*. Pt>>Ru3MC>Pd3MC>304MC. However, there was a slight decrease in the OCP for Pt and a considerable decrease in OCP for the other alloys in comparison to those obtained under aerated conditions. In terms of the temperature and oxygen concentrations, the trends observed for the different alloys are more apparent when the OCP is plotted against the PGM concentration for the different conditions (*see* Figure 6)

(a)

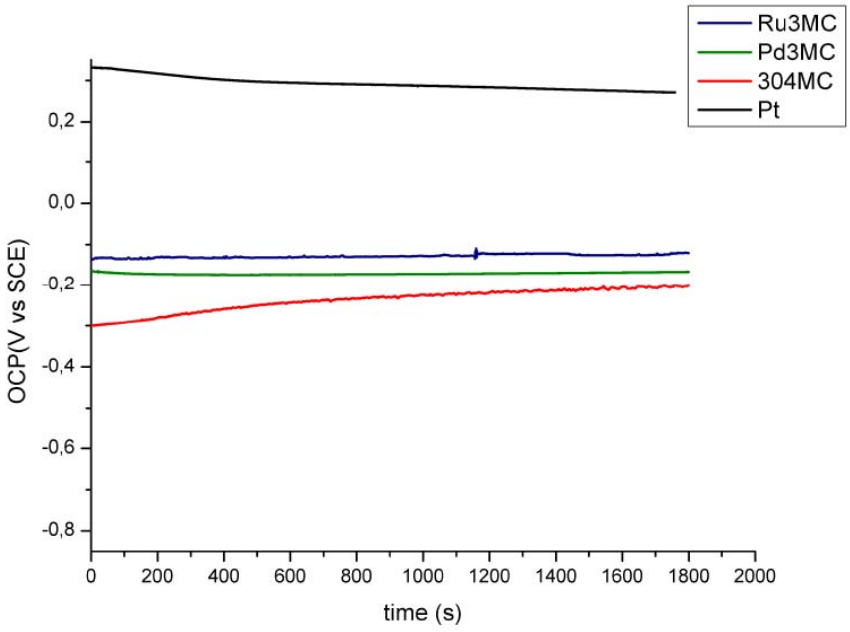

(b)

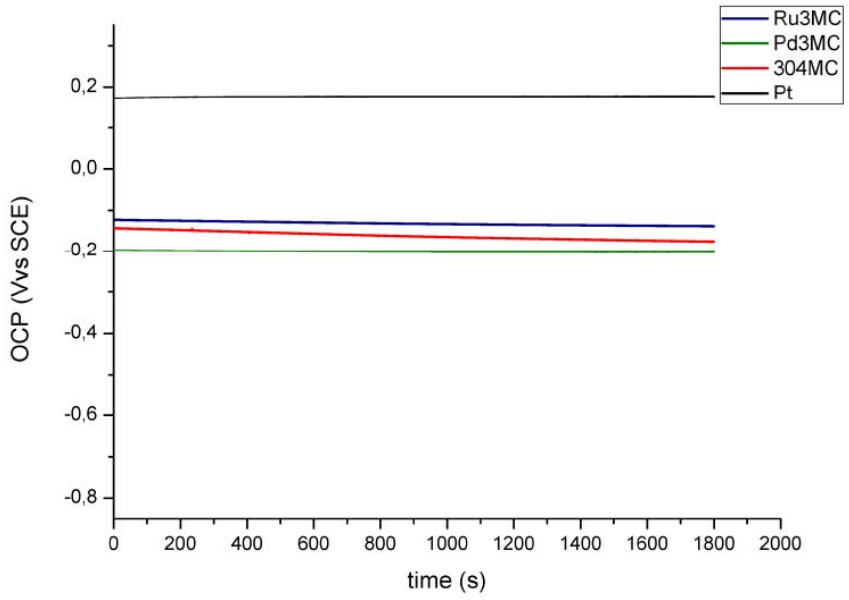

Figure 5 Open circuit potentials for various alloys in a solution containing 1000 ppm B + 2 ppm Li at (a) 25°C in aerated environment; (b) 70°C in aerated environment.

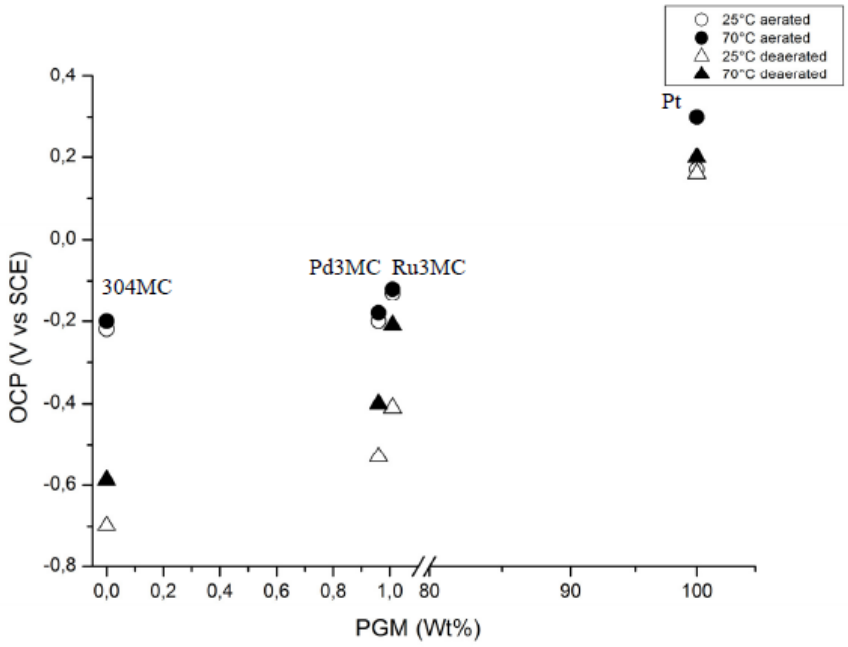

Figure 6: Graph representing the OCP against the PGM concentration in aerated and deaerated environments and at 25°C and 70°C in a solution containing 1000 ppm B + 2 ppm Li

The polarisation scans for pure Pt, the PGM-doped alloys and 304SS were recorded from -0.3 V_{SCE} to +1 V_{SCE} *vs* OCP at a scan rate of 1 mV s^{-1} and is shown in Figure 7 and Figure 8. As shown in Figure 7(a), under aerated conditions at 25 °C, Pt demonstrates the most noble potential and the lowest passive current density (about 10^{-7} A cm^{-2}). As the anodic dissolution current density is not always apparent due to spontaneous passivation in some alloys, the passive current densities are compared. Ru addition improves the corrosion resistance as the observed passive current density (~2 x 10^{-7} A cm^{-2}) is lower than that of the standard alloy 304MC (10^{-6} A cm^{-2}). Similarly, Pd also results in a lower passive current density but the effect is less significant than for Ru additions. For the reactions carried out at 70 °C under aerated conditions (Figure 5b), a similar pattern of results was obtained. Polarisation scans were also obtained under deaerated conditions at 25°C and 70°C (Figure 8(a) and (b) respectively) and it was found that decreased oxygen levels led to much lower OCP values, although a similar trend was observed for the passivation current densities as found under aerated conditions.

(a)

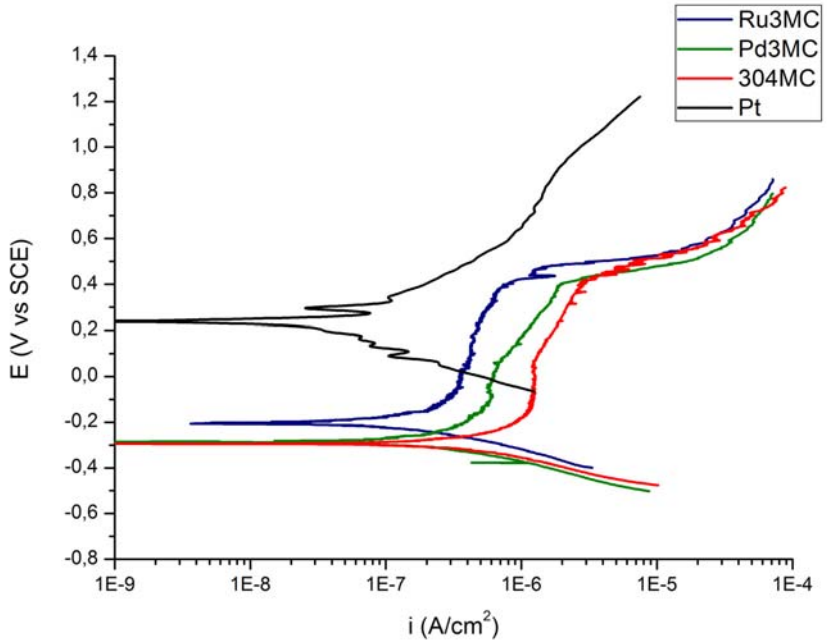

(b)

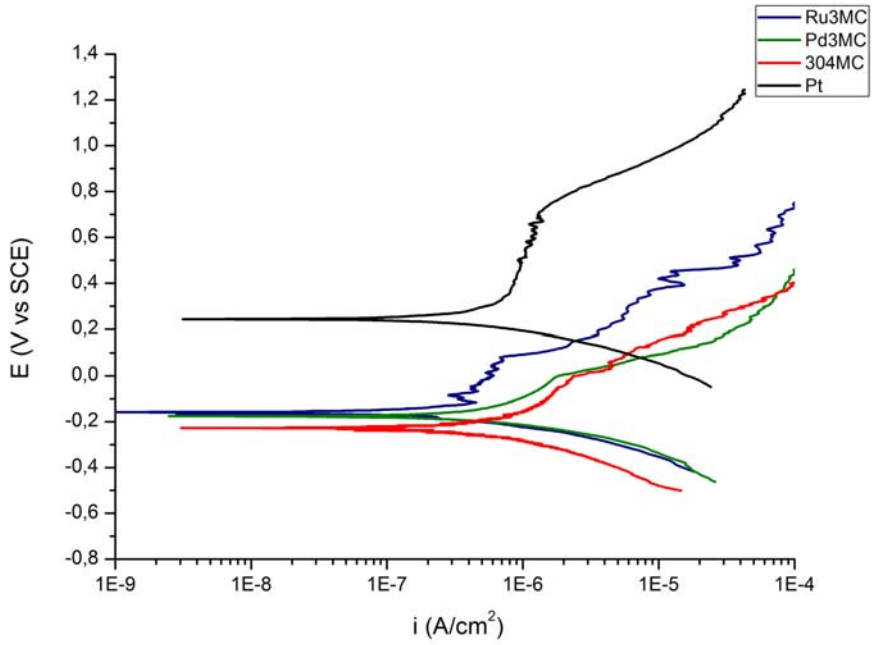

Figure 7: Polarisation scans for various alloys in a solution containing 1000 ppm B + 2 ppm Li in aerated environment at (a) 25°C and (b) 70°C.

(a)

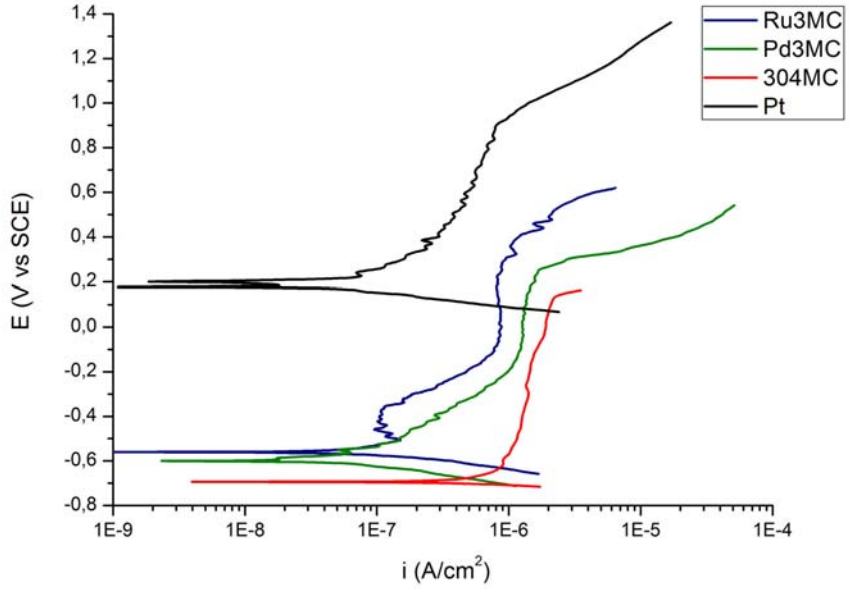

(b)

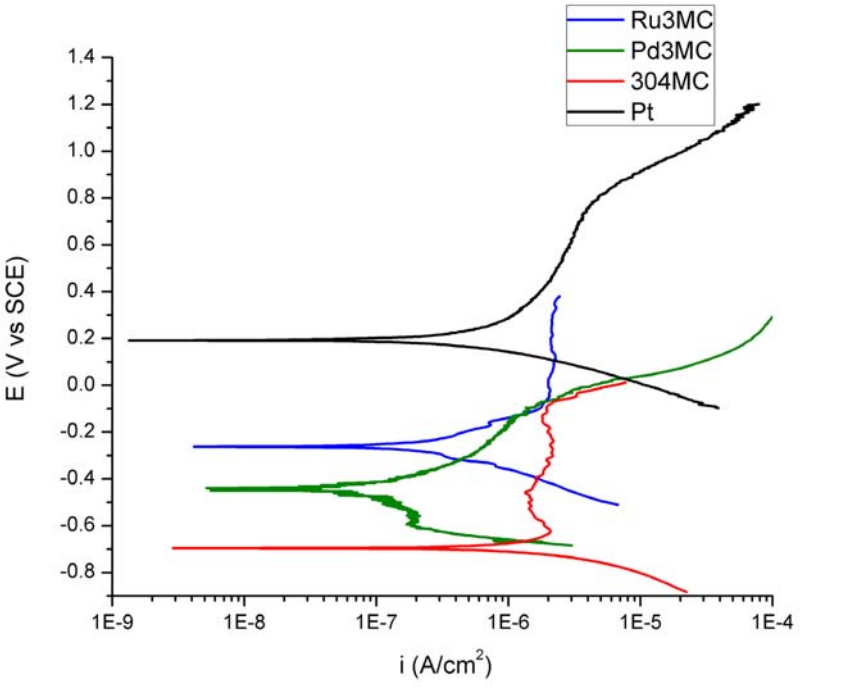

Figure 8: Polarisation scans for various alloys in a solution containing 1000 ppm B + 2 ppm Li in deaerated environment at (a) 25°C and (b) 70°C.

In order to demonstrate the effect of both temperature and oxygen on the anodic behaviour of the alloys, the polarisation curves of the Ru-modified alloy obtained under the various test conditions is given in Figure 9. A similar pattern of results has been observed for all the alloys investigated in this study. An increase in temperature from 25°C to 70°C increases the OCP, whilst at any given temperature, increasing the oxygen concentration also increases the OCP. Under aerated conditions, an increase in temperature did not demonstrate a significant change in terms of the passive current density but showed a decrease in the size of the passive region. In addition, the onset of the transpassive region occurs at lower potentials at 70°C than 25°C. Under deaerated conditions, on the other hand, the passive current density is much higher at 70°C than at 25°C and the passive region also appears smaller at this temperature.

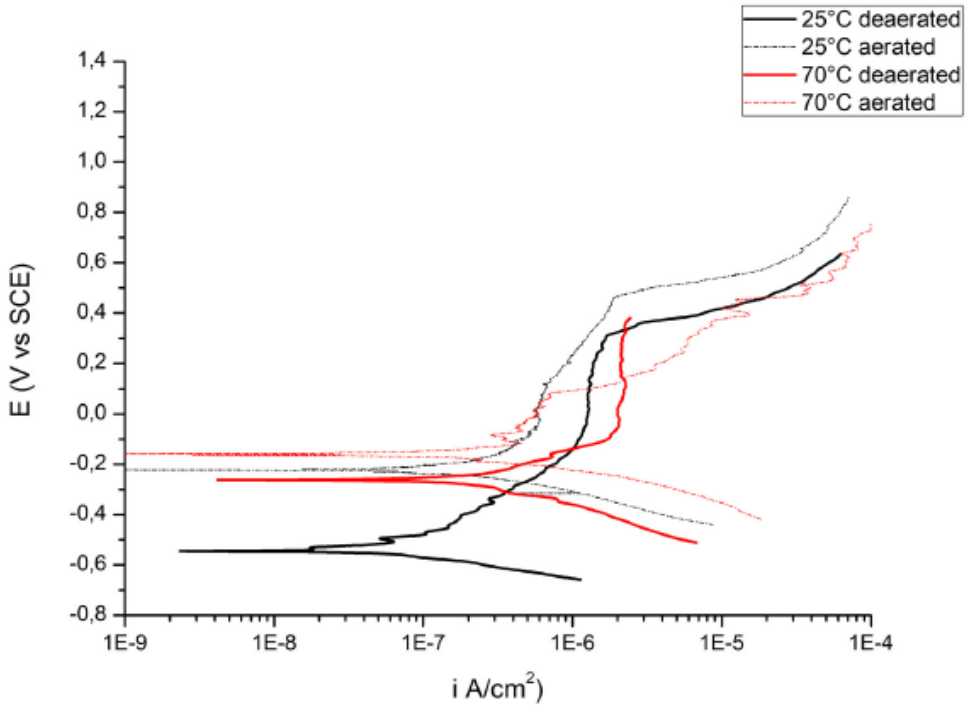

Figure 9: Polarisation scan of 1% Ru alloy (Ru3MC) in a solution containing 1000 ppm B + 2 ppm Li in aerated (dashed lines) and deaerated (solid lines) at 25°C (black) and 70°C (red).

The influence of the ruthenium concentration on the electrochemical behaviour, under both aerated and deaerated conditions, in lithiated and borated water was studied. The OCP of the Ru-doped alloys (Ru1MC, Ru2MC and Ru3MC) and 304MC, under aerated conditions at 25°C, was measured against a saturated calomel electrode (SCE) for 30 minutes. The results are shown in Figure 10. In aerated conditions, the open circuit potential was relatively stable over a

30 minute period, the small variations between the Ru-containing alloys are not considered particularly significant, although it is significant that they are more noble than the standard alloy (304MC).

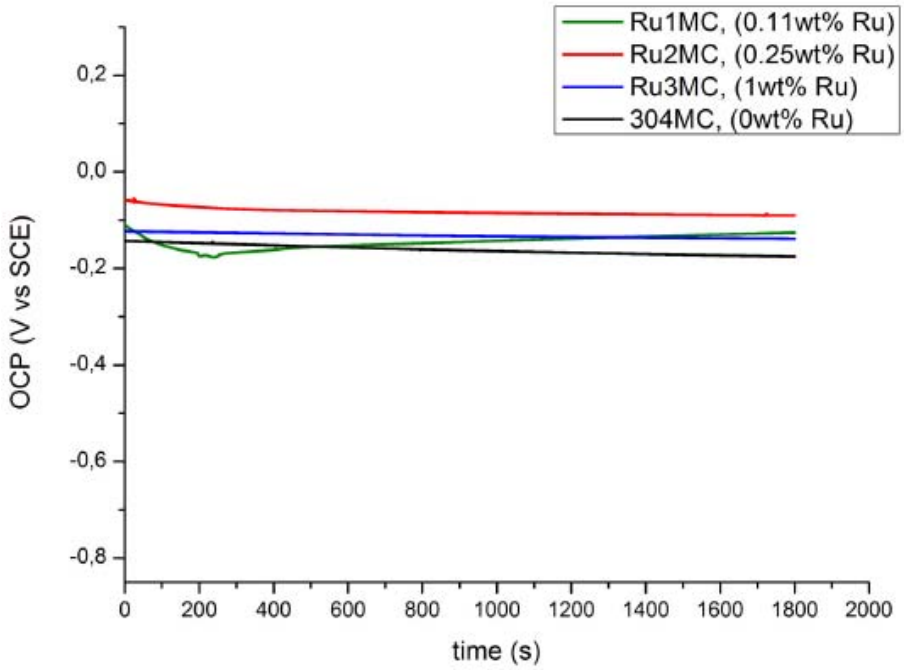

Figure 10: Open circuit potential in a solution containing 1000 ppm B + 2 ppm Li at 25°C in aerated environment: Ru1MC (green solid line), Ru2MC (red solid line), Ru3MC (blue solid line), 304MC (black solid line)

The potentiodynamic scans under aerated and deaerated conditions at 25°C were recorded against a SCE from -0.3 V below the OCP to +1 V above the OCP. The results for Ru1MC, Ru2MC, Ru3MC and the standard alloy 304MC are presented in Figure 11 and Figure 12. From Figure 11, it is clear that Ru additions to 304SS significantly influence the anodic electrochemical behaviour of the alloy. Thus, the active anodic peak is absent, implying spontaneous passivation, with the effect most prominent with 0.25% Ru, *i.e* Ru2MC. There appears to be little difference in the passive current densities between the alloys modified with 0.25 and 1 wt. % Ru.

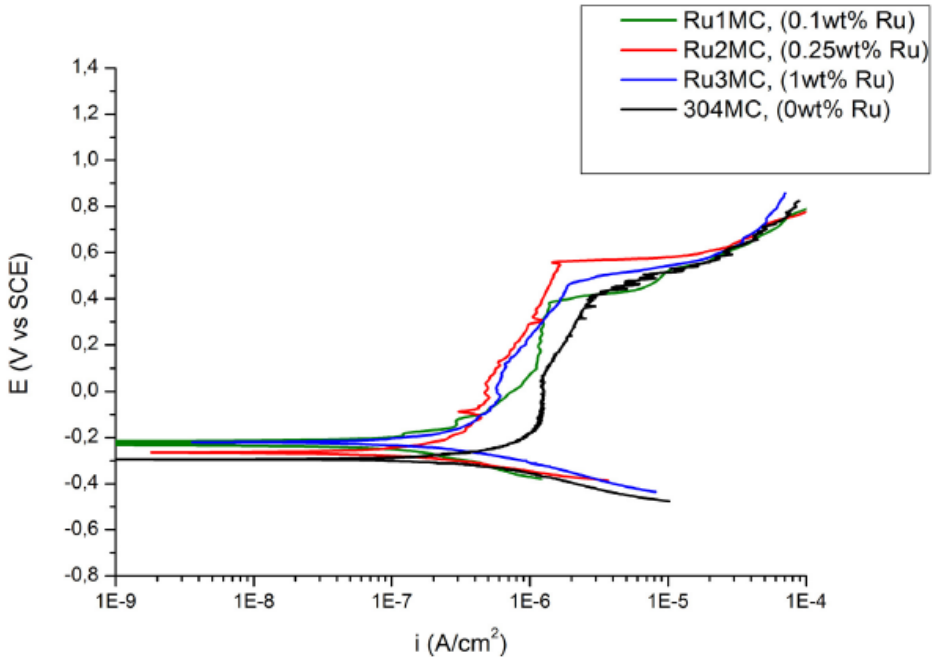

Figure 11 Polarisation of Ru-doped alloys in aerated 1000ppm B + 2ppm Li at 25°C.

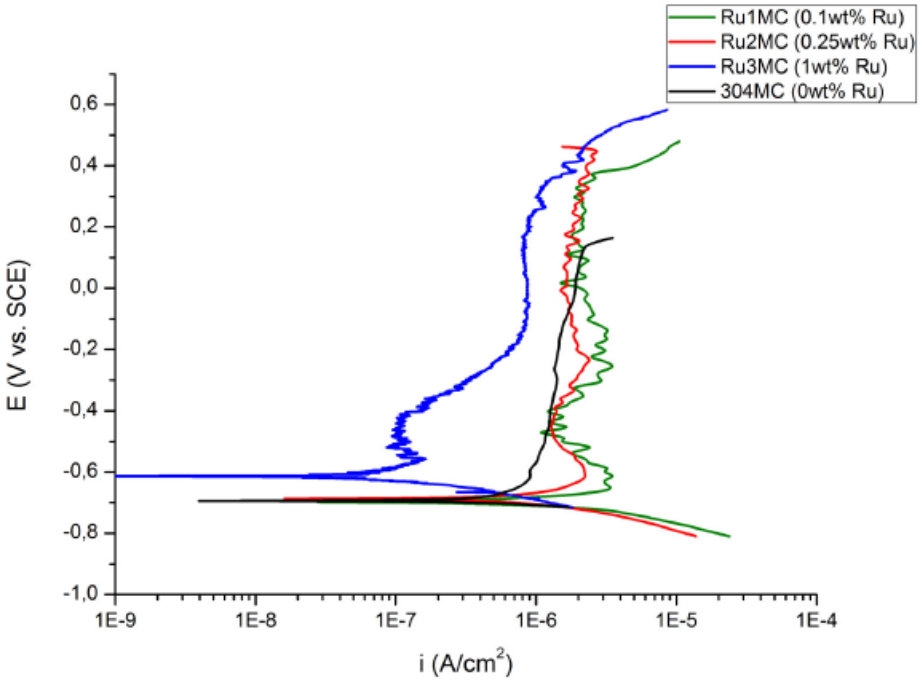

Figure 12 Polarisation scan of Ru doped alloys in dearated 1000ppm B + 2ppm Li at 25°C:

The effect of ruthenium on the electrochemical behaviour of the alloys under deaerated conditions is shown in Figure 12. In general, it was found that the alloys with 0.11 and 0.25 wt. % Ru had similar OCP values as the 304MC under deaerated conditions at 25°C. However, the higher ruthenium content had a slightly elevated OCP but a significantly decreased (by ten times) anodic dissolution rate.

Subsequent experiments in the same electrolyte were carried out under hydrogenated conditions. The study focussed on the effect of hydrogen, which plays a significant role in controlling the electrochemical potential and mitigating IGSCC in PWRs. The OCP of the alloys were obtained for 30 minutes at 25°C under hydrogenated conditions and compared to that of pure Pt under the same conditions. This is shown in Figure 13.

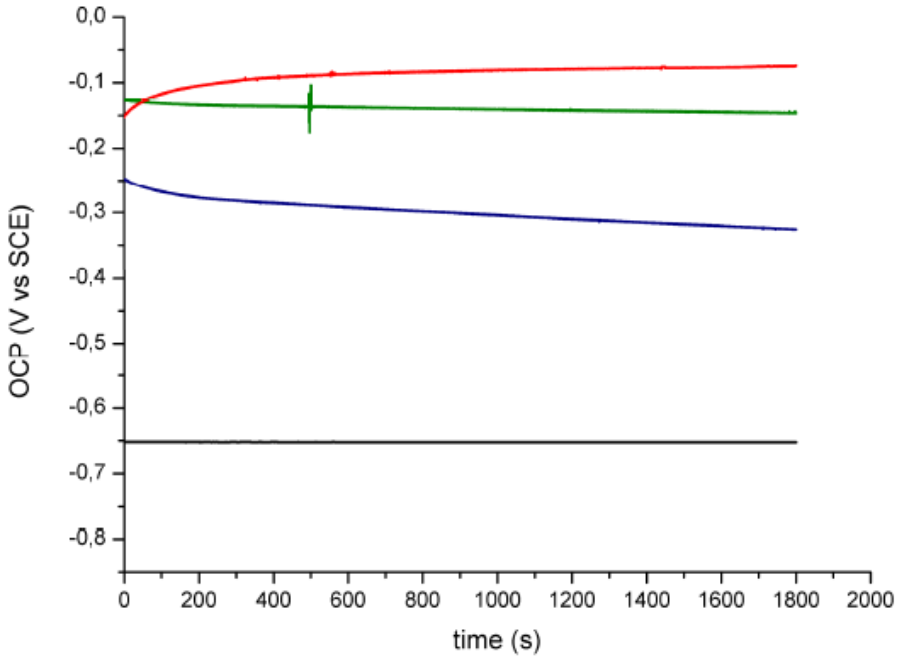

Figure 13 Open circuit potential in a solution of (1000 ppm B + 2 ppm Li) at 25°C in hydrogenated environment: Ru3MC (solid blue line), Pd3MC (solid green line), 304MC (solid red line), Pt (solid black line)

The OCP for Pt was stable over 30 minutes, and corresponds to the equilibrium value for the hydrogen evolution reaction (and, hence, the thermodynamically preferred value). In contrast the OCP of 304MC increased slightly over this period. The OCP of the PGM-containing alloys lay between the standard alloy and Pt. Significantly, the ruthenium-doped

alloy has a more negative (and preferred) potential indicating its effectiveness under these conditions.

The potentiodynamic scan in hydrogenated conditions at 25°C was measured against a saturated calomel electrode (SCE) from -0.3V below the OCP to +1V above the OCP. The results for pure Pt, the PGM-doped and the standard alloy are presented in Figure 14.

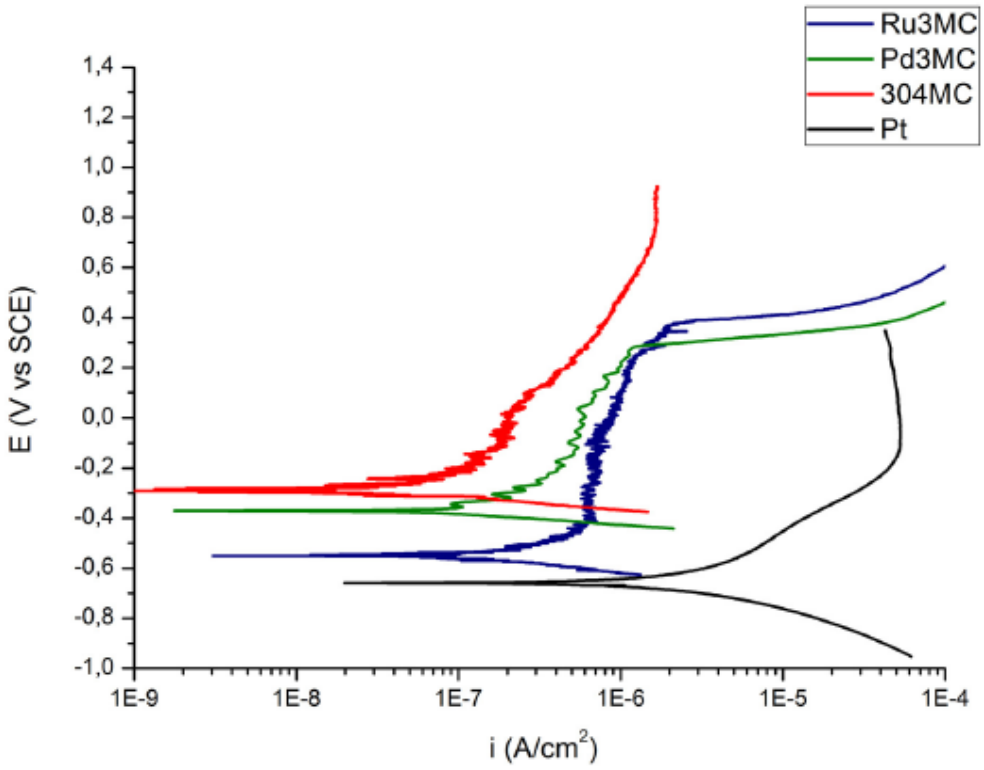

Figure 14: Potentiodynamic scan in hydrogenated 1000ppm B + 2ppm Li at 25°C: Ru3MC (solid blue line), Pd3MC (solid green line), 304MC (solid red line), Pt (solid black line)

From Figure 14, it is obvious that PGM additions to 304SS lowered the OCP and increased the anodic current density under hydrogenated conditions. The order for the OCP was as follows: Pt< Ru3MC, <Pd3MC<304MC. This was consistent with the results presented in Figure 13. Again, the ruthenium doped alloy (compared with the standard alloy) shows a potential relatively close to the thermodynamic equilibrium for hydrogen evolution; this is the preferred position for the material where the risk of SCC is minimised.

The effect of Ru concentration has been investigated in more detail as Ru3MC seemed to show better performance than Pd3MC in terms of catalysing for the hydrogen evolution reaction. The open circuit potential for all the ruthenium doped alloys in (1000ppm B + 2 ppm

Li) under hydrogenated conditions at 25°C was recorded for 30 minutes. The results are given in Figure 15.

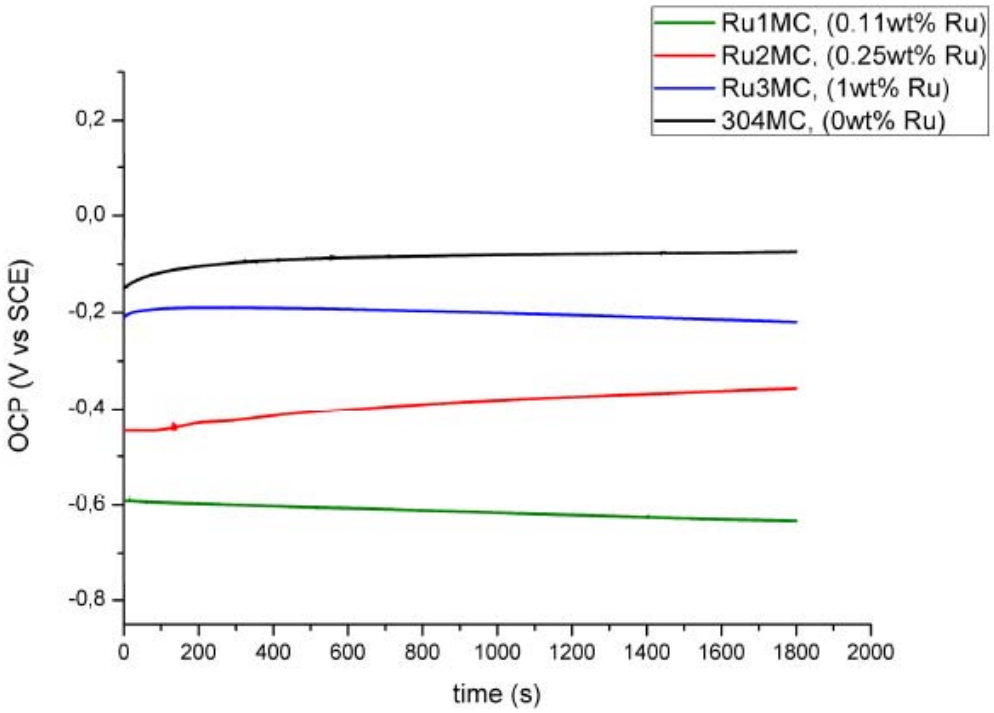

Figure 15 Open circuit potential in hydrogenated 1000 ppm B + 2 ppm Li at 25°C.

From Figure 15, the results show that under hydrogenated conditions, Ru1MC lowered the OCP ~ 6x compared to the 304MC whilst Ru2MC and Ru3MC lowered it 4 and 2 times respectively. In these environmental conditions, the OCP seemed to be stable over 30 minutes.

The potentiodynamic scan in hydrogenated conditions at 25°C was measured against a saturated calomel electrode (SCE) from -0.3V below the OCP to +1V above the OCP. The results for the Ru doped alloys are presented in Figure 16.

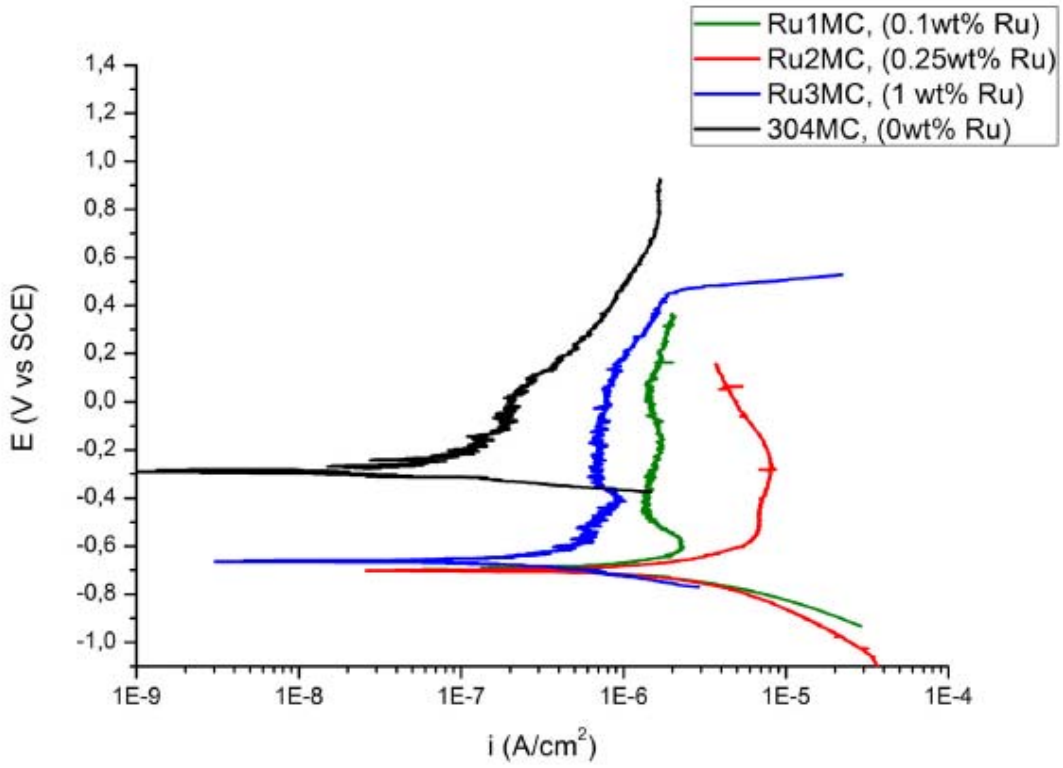

Figure 16 Polarisation of Ru doped alloys in hydrogenated 1000ppm B + 2ppm Li) at 25°C.

From Figure 16, the results confirm the beneficial effect of Ru additions on the achievement of the lowest possible electrochemical potential (OCP) under these environmental conditions.

3.1.1.2 High-temperature electrochemical tests

Under deaerated conditions, four sets of experiments were carried out at 260°C in hydrogenated pressurised water and these results are shown in Figures 17 and 18.

.

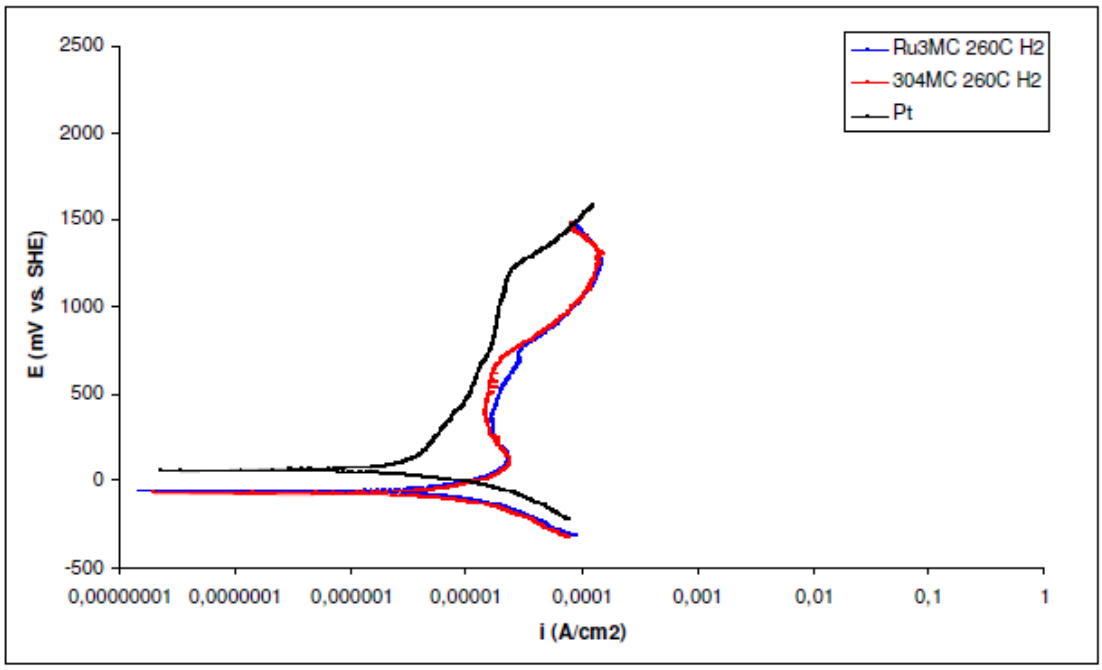

Figure 17 Polarisation measurements under hydrogenated conditions in lithiated borated water at 260°C: Pt (black line), Ru3MC (blue line), 304MC (red line)

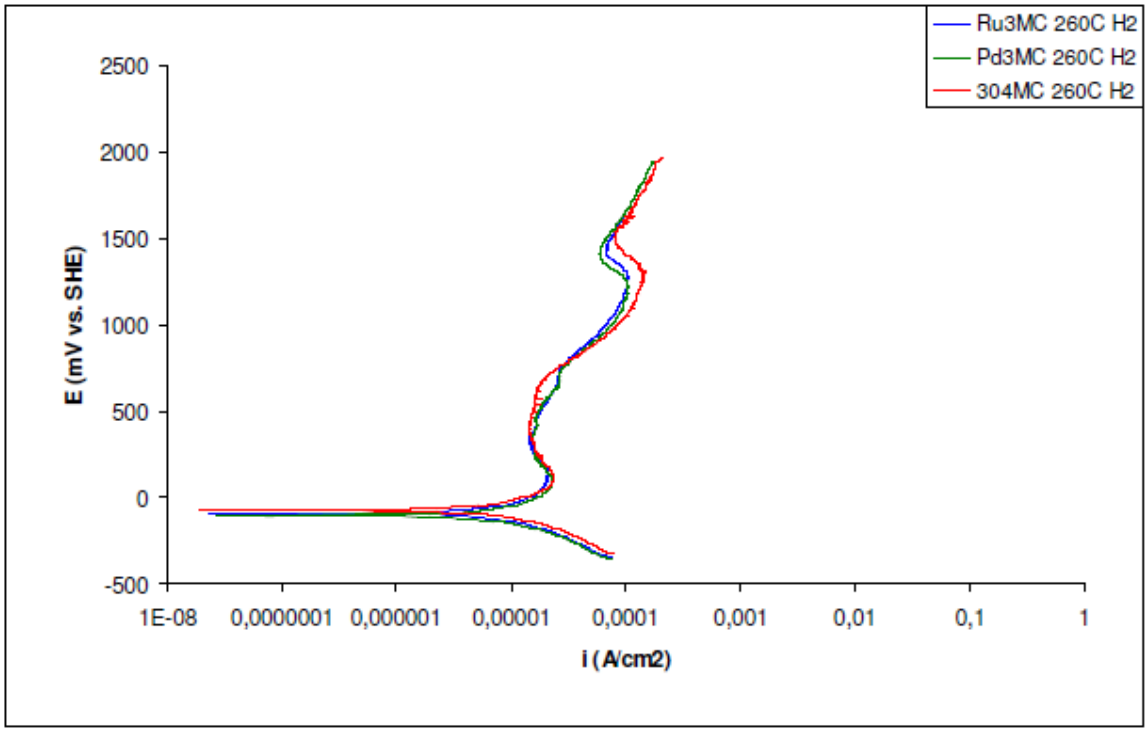

Figure 18: Polarisation measurements under hydrogenated conditions at 260°C: Pt (black line), Ru3MC (blue line), Pd3MC (green line), 304MC (red line).

The autoclave data under hydrogenated conditions show no major differences between the alloys although, and significantly, the PGM-doped alloys tended to have more negative potentials than the standard material. Regarding anodic current densities, again no major differences were observed although the ruthenium-doped alloy has a slightly lower anodic current density. These generally confirm the beneficial influence of PGM additions (particularly ruthenium) on the performance of the 304MC material that were found at lower temperatures.

3.1.2 Electrochemical measurements in acidified tetrathionate solutions

Potassium tetrathionate solution, acidified below pH 2, is generally employed as a model environment in order to promote the rapid generation of intergranular corrosion and SCC. It is germane to study whether PGM-doped alloys have notably different electrochemistry in this aggressive medium, to compare the corrosion behaviour of the three alloys, *i.e.* standard 304SS, Pd3MC and Ru3MC. The experiments were carried out in solutions of 0.01 M $K_2S_4O_6$, pH=1.5, under both aerated and deaerated conditions at 25°C. Figure 19(a) shows the OCP for the three alloys after 30 min exposure to the solution under aerated conditions. Interestingly, whilst the pure Pt showed no change in the OCP there was an abrupt increase for both the 304 standard and PGM-doped alloys; this is due to the alloy passivation process, which is clearly more efficient in the PGM-doped alloys. The change occured most rapidly in the Ru-doped 304SS (~800 s *vs*. ~ 2100 s for Pd and ~2600 s for 304MC). Under deaerated conditions at 25°C, the OCP was constant for all alloys during the 30 min run (see Figure 19b) with no notable variation in the OCP values between the 304SS and PGM-modified alloys, unlike in aerated conditions.

(a)

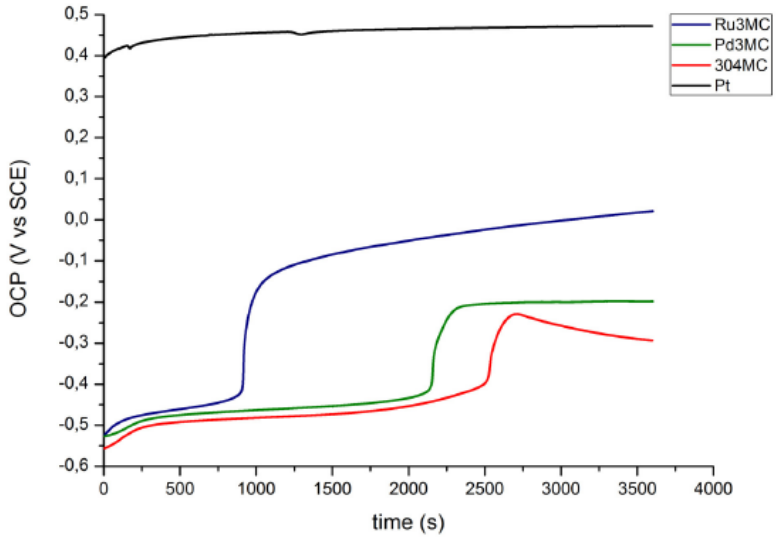

(b)

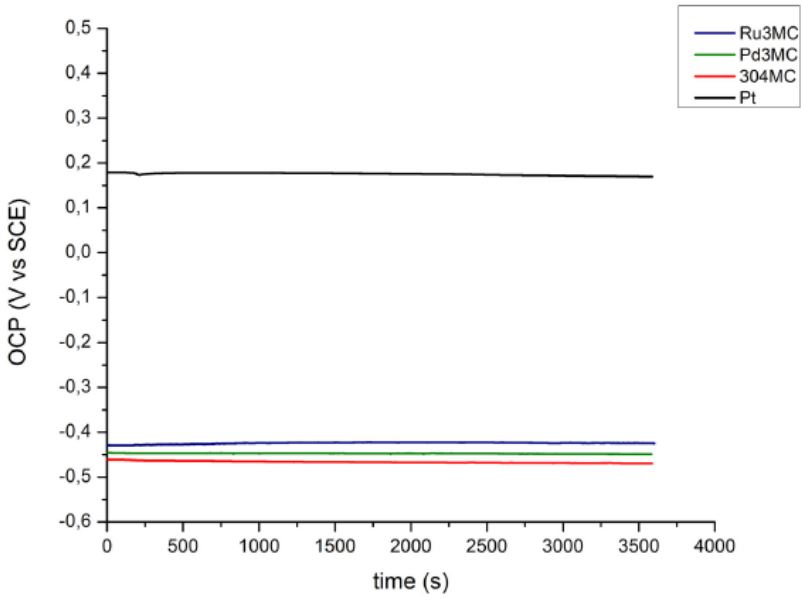

Figure 19: Open circuit potential in 0.01M $K_2S_4O_6$ at 25°C in (a) aerated environment and (b) deaerated environment.

Polarisation curves obtained under aerated conditions in 0.01 M $K_2S_4O_6$ (pH 1.5) are complex. Thus, for the curves recorded with a scan rate of 0.5 mVs^{-1}, Figure 20(a), all three alloys demonstrated an oxidation peak around −0.3 V_{SCE} prior to the anodic dissolution peak (~−0.2 V_{SCE}) and passivation. There was also a feature around 0.3 V_{SCE} for all alloys. Both

PGM-containing alloys showed almost identical behaviour with respect to the first peak at -0.3 V_{SCE} whilst in terms of the anodic/critical current density, 304SS showed the largest peak, followed by Pd and then Ru the lowest (lower being better). In terms of the passivation kinetics, the alloys followed the trend Pt>>Ru3MC>Pd3MC>304SS.

When the scan rate was increased from 0.5 mV s^{-1} to 5 mV s^{-1}, although similar features were apparent in the anodic polarisation curves and the overall trends remained similar, some distinctions are now apparent in the electrochemical behaviour of the virgin and PGM alloys. At the higher scan rate, Figure 20(b), the feature observed at ~0.3 V_{SCE} was now greatest for Pd3MC, followed by Ru3MC and then 304MC, in contrast to the rank order 304MC>Pd3MC>Ru3MC observed at the lower scan rate.

(a)

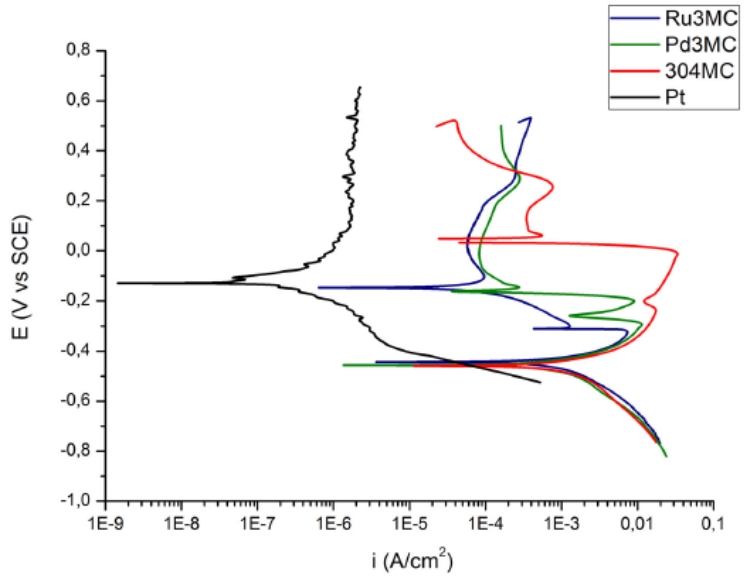

(b)

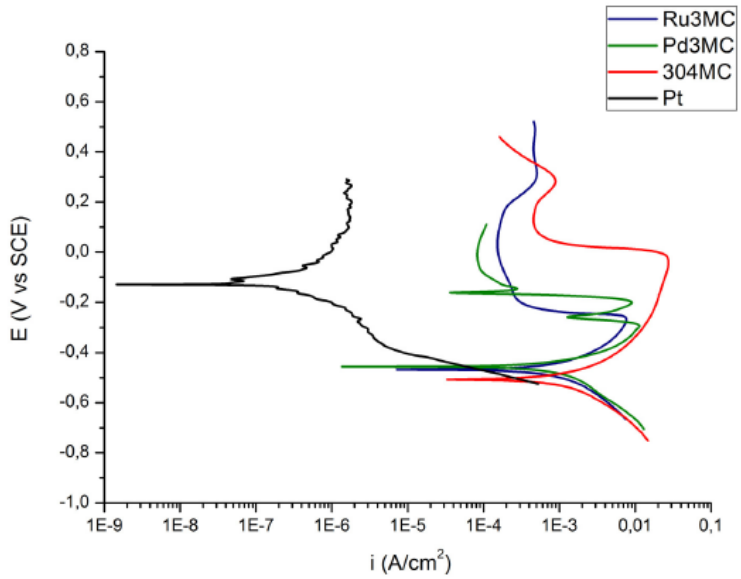

Figure 20: Polarisation scan in aerated 0.01M $K_2S_4O_6$ at 25°C with a scan rate of (a) 0.5mVs^{-1} and (b) 5mVs^{-1}.

Under deaerated conditions, the lower scan rate, Figure 21(a), showed similar trends to those curves obtained in the aerated environment, employing the same scan rate, Figure 20(a), in terms of the feature observed at ~-0.3 V_{SCE}, however, the size of the peaks for the anodic current density and the feature at ~0.3 V_{SCE} followed a different pattern to those obtained in the aerated environment. Increasing the scan rate (x10) produced a remarkable change in behaviour, as the feature at ~-0.3 V_{SCE} is no longer distinct from the dissolution current density. Furthermore, the two distinct regions in the cathodic curve were also obscured and appeared as one smooth curve. The passivation behaviour of all alloys followed a similar trend as observed previously for the other conditions. Importantly, for all conditions, the anodic currents were significantly lower for PGM-doped alloys. Since this environment is designed to attack grain boundaries, this evidence supports the interpretation that PGM-doped alloys have more resistance to intergranular corrosion than the standard alloy,

(a)

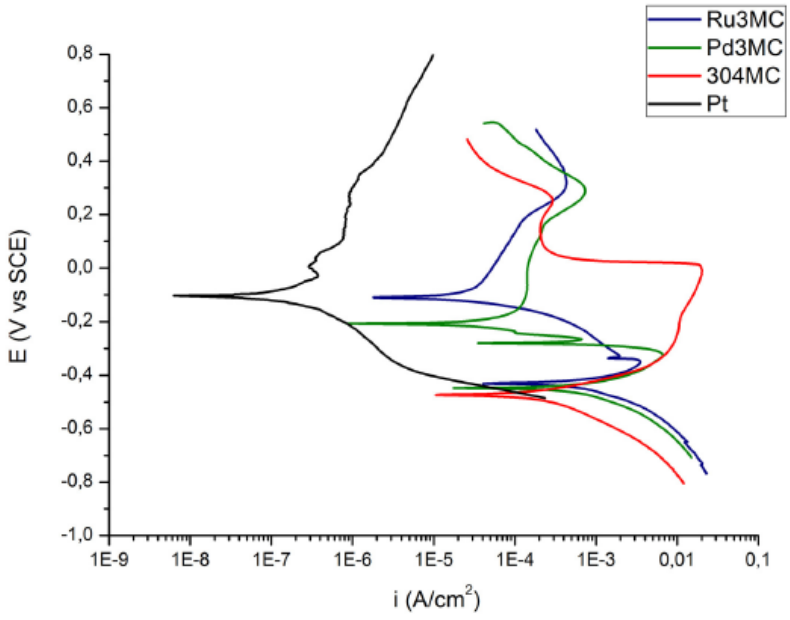

(b)

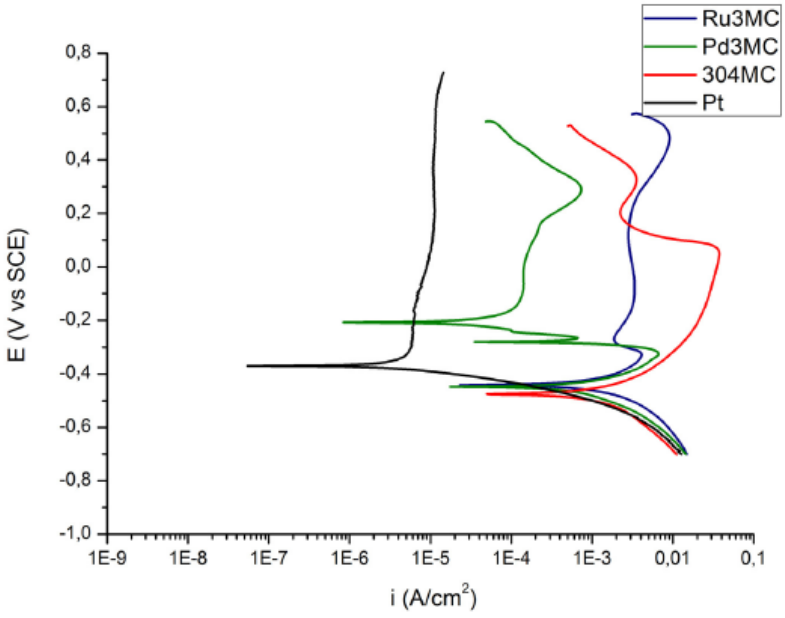

Figure 21: Polarisation scan in deaearated 0.01M $K_2S_4O_6$ at 25°C with a scan rate of (a) 0.5mVs^{-1} and (b) 5mVs^{-1}.

In order to demonstrate the effect of the scan rate on the electrochemical behaviour, the polarisation curves for the Ru3MC alloy under both aerated and deaerated conditions employing both scan rates are shown in Figure 22. A striking observation from these curves, , is that deaeration results in a significant increase in the current density of the features around ~-0.3 V_{SCE} and a decrease in the current density for the peak at 0.3 V_{SCE}.

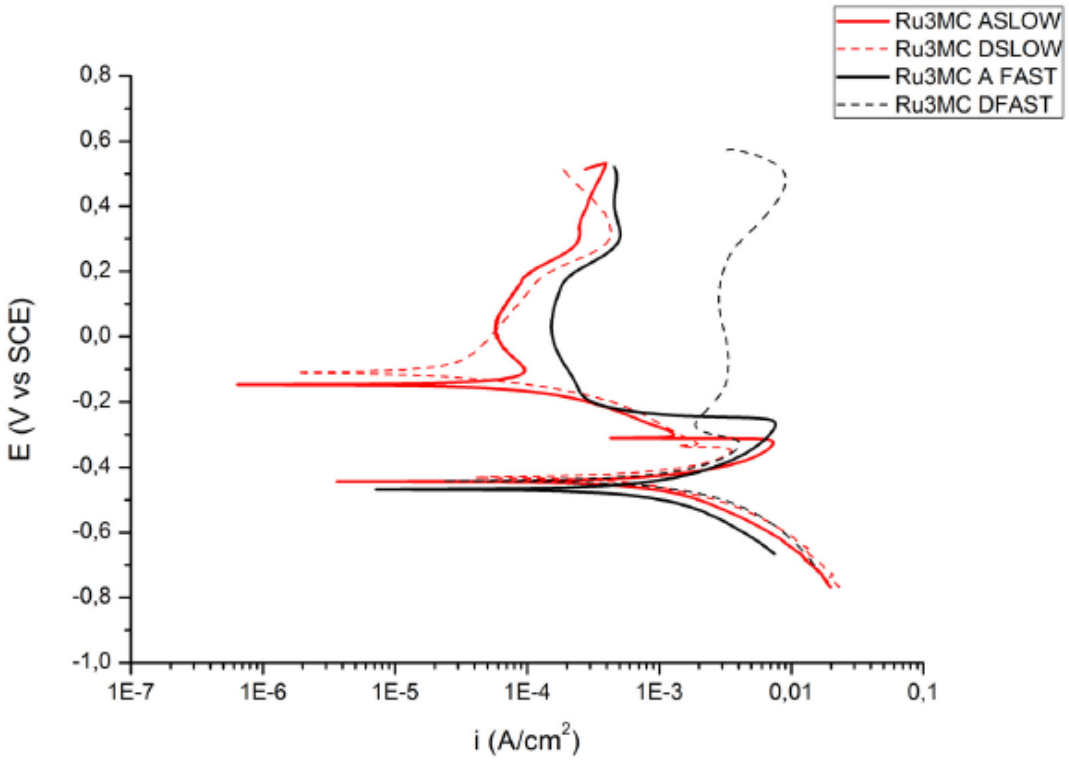

Figure 22: Polarisation scane of Ru3MC in aearated 0.01M $K_2S_4O_6$: Ru3MC at 0.5mVs-1 (red solid line), Ru3MC in deaerated environment at 0.5mVs^{-1} (red dashed line), Ru3MC in aerated environment at 5mVs^{-1} (black solid line), Ru3MC in deaerated environment at 5mVs^{-1} (black dashed line)

3.2 *Part B – Electrochemical and mechanical studies of cold worked 304L SS*

3.2.1 Electrochemical studies of CW 304L SS

3.2.1.1 Effects of Anisotropy on Electrochemical Behaviour

In order to investigate the possible effects of anisotropy, OCP and anodic potentiodynamic polarisation (APP) measurements were carried out for each material, subjected to different processing treatments, and the results compared. The results of the tests are shown in order of their increasing level of cold work. A plot of OCP against time for the annealed samples is shown in Figure 23(a). It appears that the OCP of the AN-S and AN-T were almost indistinguishable at -0.321 V_{SCE} and -0.319 V_{SCE} respectively. However, AN-L showed a relatively lower electrode potential of -0.340 V_{SCE}. This result suggested that AN-L appeared to display less noble behaviour than the AN-S and AN-T.

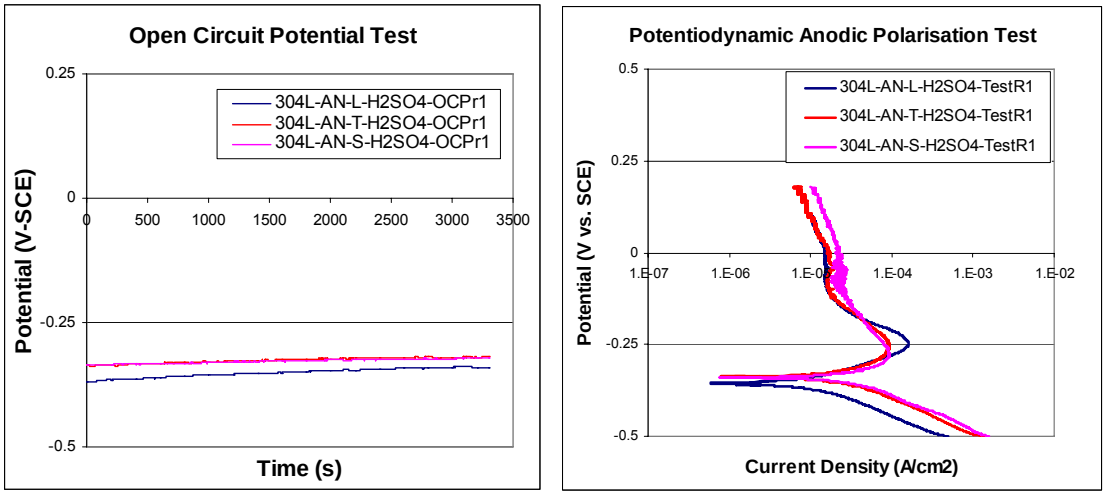

(a) (b)

Figure 23: Open circuit potential (a) and potentiodynamic polarisation (b) curves for annealed material

Figure 23(b) shows the results of electrochemical polarisation for the annealed samples. Again, the anodic dissolution peaks for the curves obtained in the AN-S and AN-T planes did not show any significant difference whilst the AN-L plane showed a larger dissolution peak.

The results of the electrochemical studies on the 5% CW sample are shown in Figure 24. The OCP results in Figure 24(a) shows that 5% CW-S has the highest value of OCP

followed by 5% CW-T and then 5% CW-L with their respective OCP values corresponding to -0.309 V_{SCE}, -0.323 V_{SCE} and -0.332 V_{SCE}. The suggested order of their nobility in terms of their OCP values with respect to their plane normal is S>T>L. The polarisation curves for the 5% CW samples are shown in Figure 24(b). The anodic dissolution peak is smallest for 5% CW-S whilst the current densities were larger and similar in value in 5% CW-T and 5% CW-L.

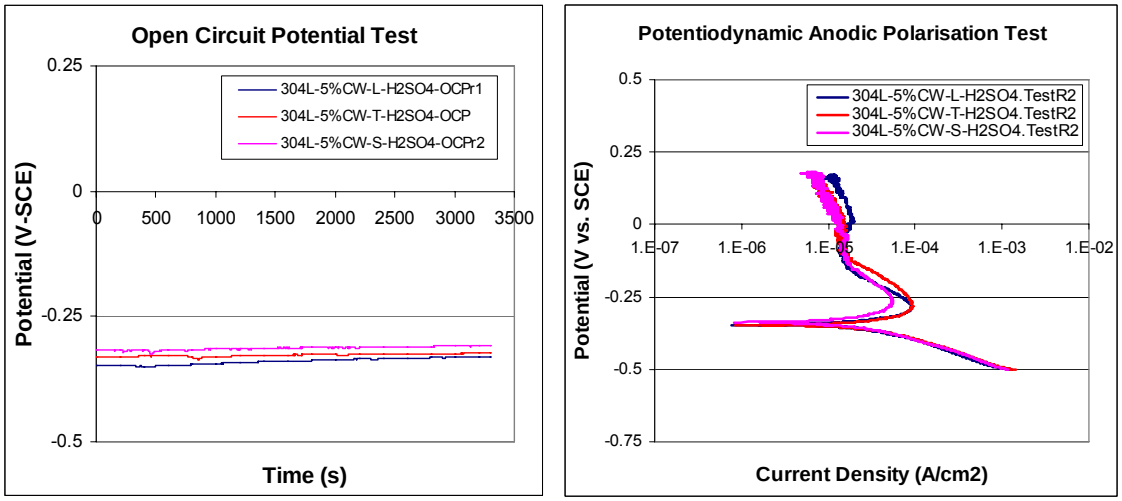

(a) (b)

Figure 24: Open circuit potential (a) and potentiodynamic polarisation (b) curves for 5% cold worked material

The results of the OCP for the 10% CW alloy, shown in Figure 24(a), appeared to beis consistent with those for the 5% CW and displayed a similar trend. The 10% CW-S has the highest electrode potential and 10% CW-L the lowest. The OCP for 10% CW-S, 10% CW-T and 10% CW-L are -0.306 V_{SCE}, -0.312V_{SCE} and -0.335V_{SCE} respectively. Figure 25(b) displays polarisation curves for the 10% CW samples. In contrast to the 5% CW alloys, the anodic dissolution peak is significantly larger for 10% CW-L. This was followed by 10% CW-T which is only slightly greater than for 10% CW-S.

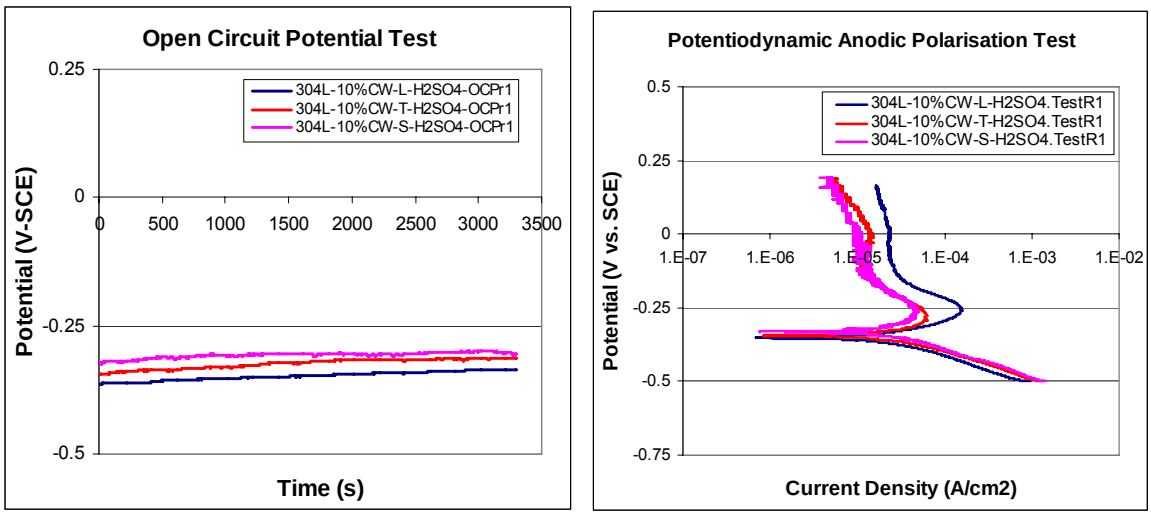

(a) **(b)**

Figure 25: Open circuit potential (a) and potentiodynamic polarisation (b) curves for 10% cold worked material

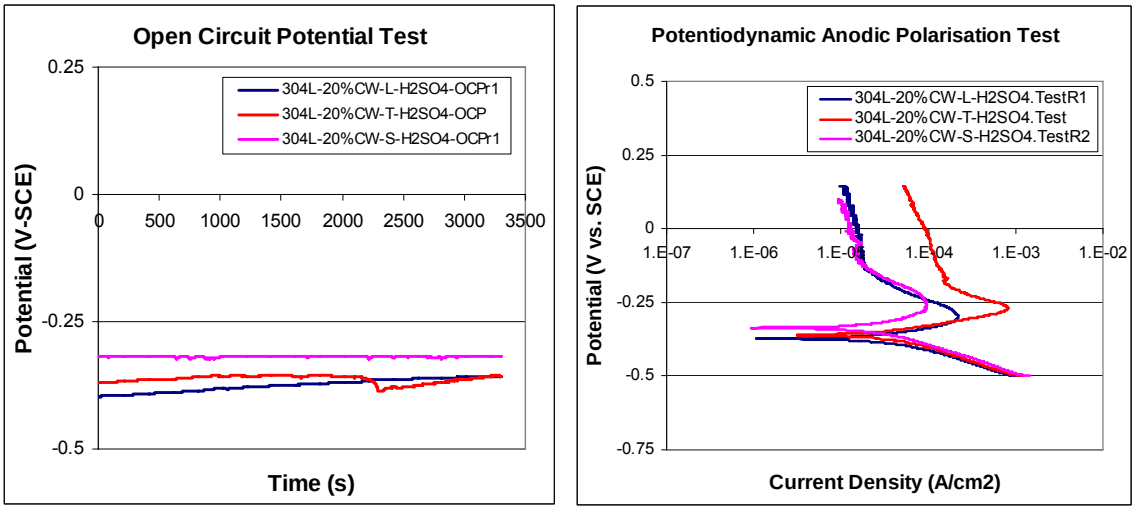

(a) **(b)**

Figure 26: Open circuit potential (a) and potentiodynamic polarisation (b) curves for 20% cold worked material

The OCP *vs*. time plots for the 20% CW material are shown in Figure 26(a). As before, 20% CW-S has the highest electrode potential followed by 20% CW-T and 20% CW-L, with the correspondent values of -0.318 V_{SCE}, -0.370 V_{SCE} and -0.397 V_{SCE} respectively. The dip in the OCP curve for the 20% CW-T was interpreted as experimental error during the test as the curve later returned back to its original value. The order of nobility is S>T>L still in line with

the earlier results. However, contrary to the OCP and the earlier results shown, the APP for the 20% CW showed a different pattern of results. The anodic dissolution peak for 20% CW-T appeared to be the greatest, in contrast to what has been observed for the other cold worked alloys above. In terms of the size of the anodic dissolution peak, 20% CW-T was followed by 20% CW-L and then 20% CW-S.

The results of the OCP and APP for 40% CW are shown in Figure 27. The electrode potentials for the 40% CW-S, 40% CW-T and 40% CW-L are -0.309 V_{SCE}, -0.328 V_{SCE} and -0.341V_{SCE} respectively, Figure 27(a). In terms of the OCP, the order of nobility follows the trend S>T>L which is also consistent with the earlier results. From the APP curves for the 40 % CW material, Figure 27(b), it is apparent that a similar trend in the anodic behaviour is observed to the annealed specimen and those alloys subjected to the lower levels of cold work (5-10 %), however, the anodic dissolution peaks for the specimens in the three orientations show very different current density values.

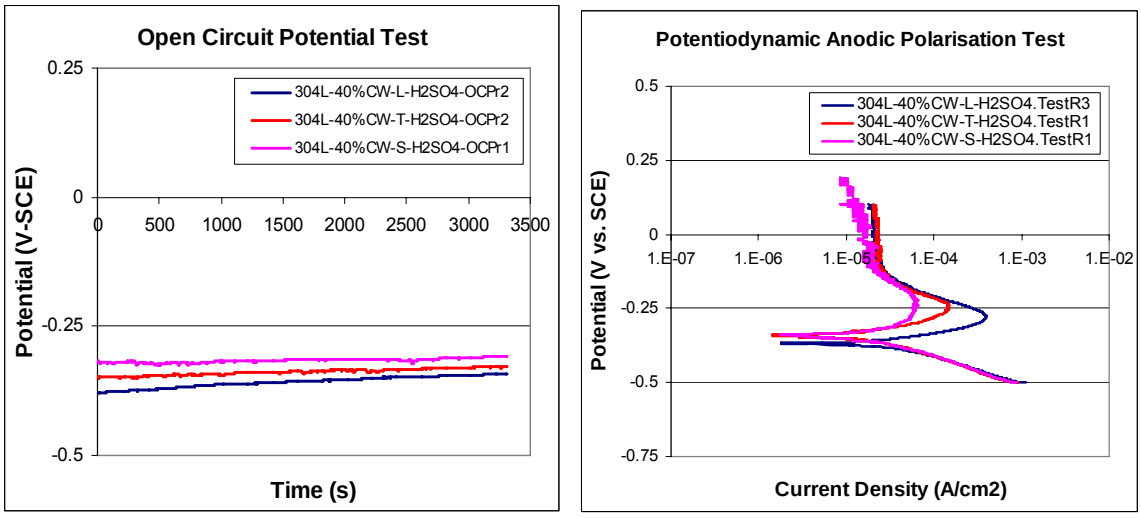

(a) **(b)**

Figure 27: Open circuit potential (a) and potentiodynamic polarisation (b) curves for 40% cold worked material

3.2.1.2 Effects of Cold Work on Electrochemical Behaviour

The effects of cold work on electrochemical behaviour were also assessed by comparing the electrochemical results obtained along the same sample orientations for the annealed sample as well as those subjected to different level of cold-reduction. The OCP values obtained for

alloys subjected to different treatments is given in Table 3. The effects of the cold work on the electrochemical behaviour of the material along the three orthogonal directions are as follow:

(a) Longitudinal Direction

The results of the open circuit potentials and polarisation curves for the alloys subjected to different processing treatments, with planes normal along the L-direction, are shown in Figures 28(a) and (b) respectively.

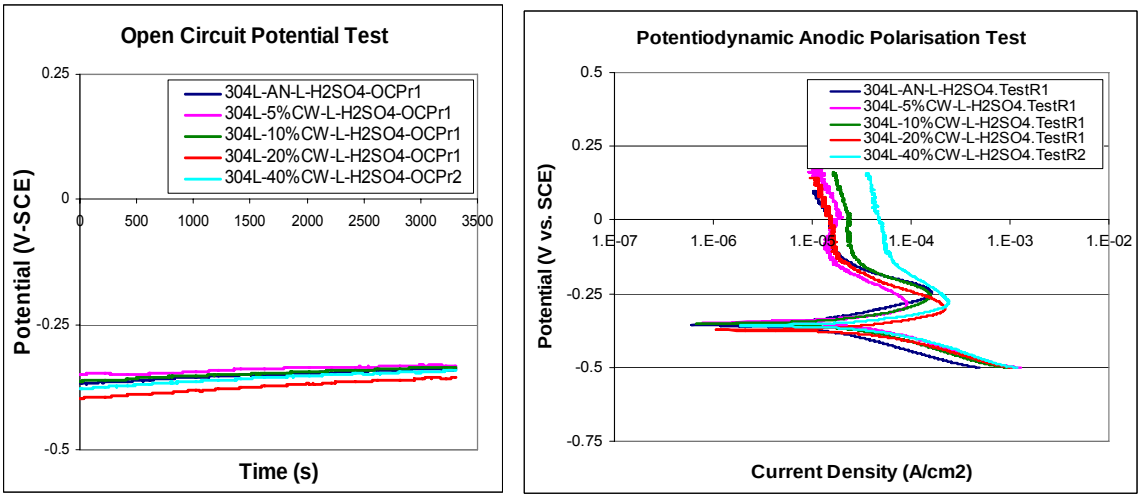

(a) **(b)**

Figure 28: Open circuit potential (a) and potentiodynamic polarisation (b) curves for planes normal to the L-direction

From the OCP results in Figure 28(a), 5% CW-L has the highest electrochemical potential in all the test samples. The electrode potential for the 10% CW-L and AN-L are almost identical and only slightly lower than the 5% CW specimen. This is followed closely by the 40% CW alloy whilst the results show that 20% CW-L has the lowest OCP which is significantly lower than all the other alloys along the same orientation. In terms of .OCP, the order of nobility can be summarised as 5% CW>10% CW> Annealed> 40% CW > 20% CW, all with the plane normal to the L-direction.

The polarisation results for all the material conditions are shown in Figure 28(b). In terms of the size of the anodic dissolution peak, the alloys follow the trend 40% CW>20% CW>10% CW=AN>5% CW.

(b) Transverse Direction

The effect of cold work on the electrochemical behaviour of all the alloys, subjected to different processing condition, with the plane normal to the T-direction is shown in Figure 29. The order of nobility is less obvious from the OCP results, Figure 29(a), as all alloys displayed similar OCPs. The electrochemical potential for the 5% CW-T and AN-T appear to be the most noble while the 20% CW-T and 40% CW are ranked the lowest on the list.

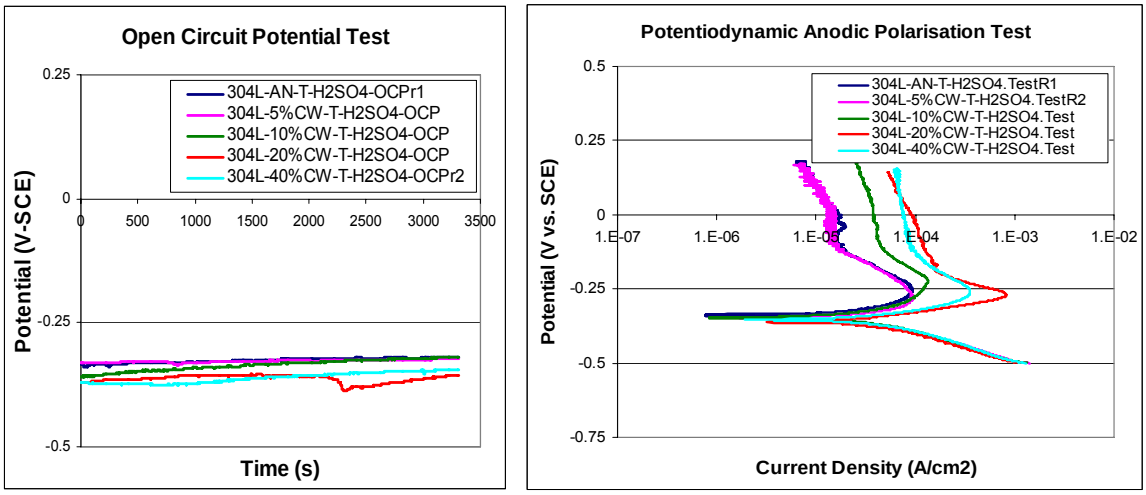

(a) **(b)**

Figure 29: Open circuit potential (a) and potentiodynamic polarisation (b) curves for planes normal to the T-direction

In contrast to the OCP results, the polarisation results, Figure 29(b) showed an apparent distinction in anodic behaviour for the alloys subjected to different processing conditions along the T-direction. The anodic dissolution peaks for the 5% CW-T and AN-T appeared to quite similar and the lowest in terms of size. This was followed by 0% CW-T, 40% CW-T and then 20% CW-T.

(c) Short-Transverse Direction

The plot of OCP *vs.* time in Figure 30(a) shows no significant effects of the cold work on the electrochemical potential along the S-direction. The electrochemical potential for all the alloys subjected to different processing conditions appeared quite close to each other and indeed overlapped. However, a closer look at the data revealed the order of nobility as thus: 10% CW>5% CW>40% CW>20% CW>AN all along the S-direction.

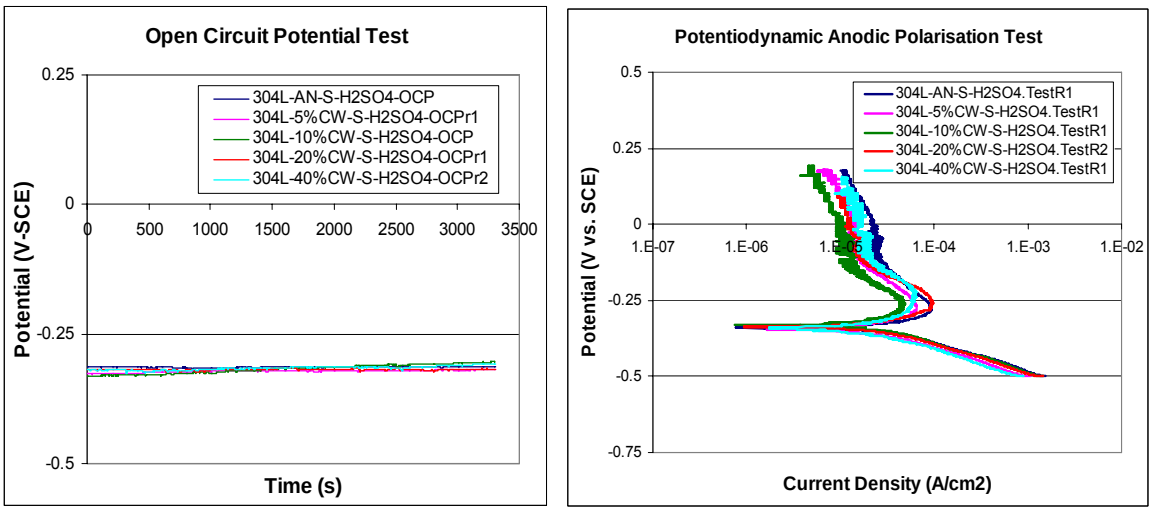

(a) **(b)**

Figure 30: Open circuit potential (a) and potentiodynamic polarisation (b) curves for planes normal to the S-direction

Figure 30(b) displays the anodic polarisation curves for alloys subjected to different processing conditions with planes normal to S-direction. The 10% CW-S showed the smallest anodic dissolution peak while the 20% CW-S and AN-S showed the largest anodic current densities. Overall, the effect of cold work on the electrochemical behaviour along the S-direction, for materials subjected to different conditions did not show any significant trends.

Table 3 Table of Summary Results

Sample	Electrode Potential (V_{SCE})
AN-L	- 0.340
AN-T	- 0.319
AN-S	- 0.321
5% CW-L	- 0.332
5% CW-T	- 0.323
5% CW-S	- 0.309
10% CW-L	- 0.335
10% CW-T	- 0.312
10% CW-S	- 0.306
20% CW-L	- 0.397
20% CW-T	- 0.370
20% CW-S	- 0.318
40% CW-L	- 0.341
40% CW-T	- 0.328
40% CW-S	- 0.309

3.2.3 Mechanical studies of cold worked 304L SS

3.2.3.1 Vickers Hardness Measurement

The result of hardness measurement is shown in Figure 31. The effect of cold work and the possible effect of anisotropy on the hardness are demonstrated. Overall, the hardness increases with the level of cold work, rising by 50 kg/m^2 per increase in cold work level. The trend of the hardness profile was rather uniform in all alloys. The regions of the material closed to the roller showed higher hardness with a saddle at the central region which has a relatively lower hardness value.

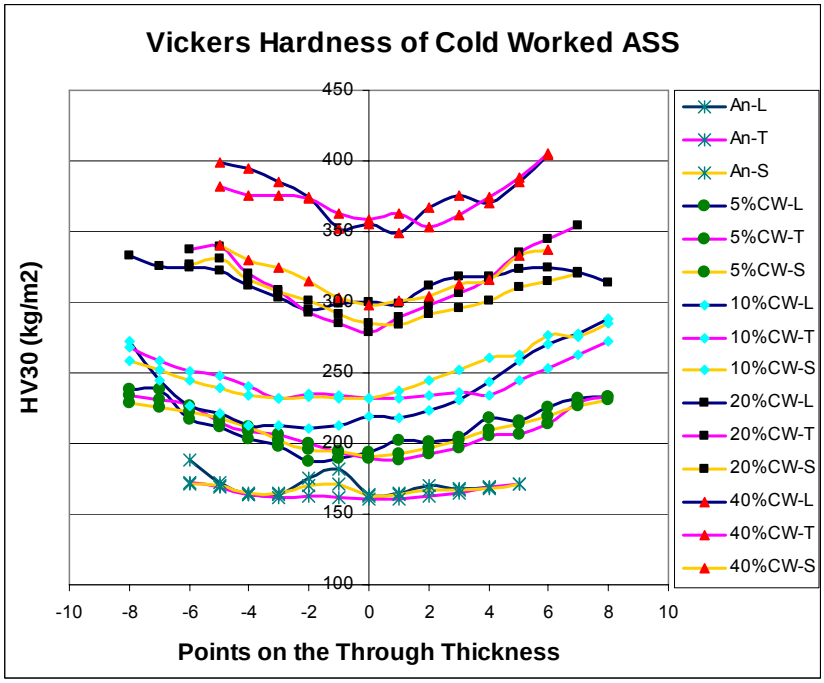

Figure 31: Hardness profiles along the L, T and S directions

The effect of microstructural orientation on the hardness values appears to be relatively low apart from the 40% CW material where the hardness along the short-transverse direction was significantly lower than in the other (L and T) directions.

3.2.3.2 Mechanical Testing

Mechanical tests were performed to investigate the effect of strain path and cold work on the yield strength of the materials. The results of stress-strain tests carried out on the annealed and cold worked materials (*viz*. 5% CW, 10% CW, 20% CW and 40% CW) are as follows:

(a) Annealed

The load cycle tests carried out on the annealed material are shown in Figure 32. In tension-tension loading cycle, the yield strength of the material was around 290 MPa during the initial tensile loading to 10 % strain; this increased to around 475 MPa when the material was reloaded to an additional 5 % tensile Figure 32(a).

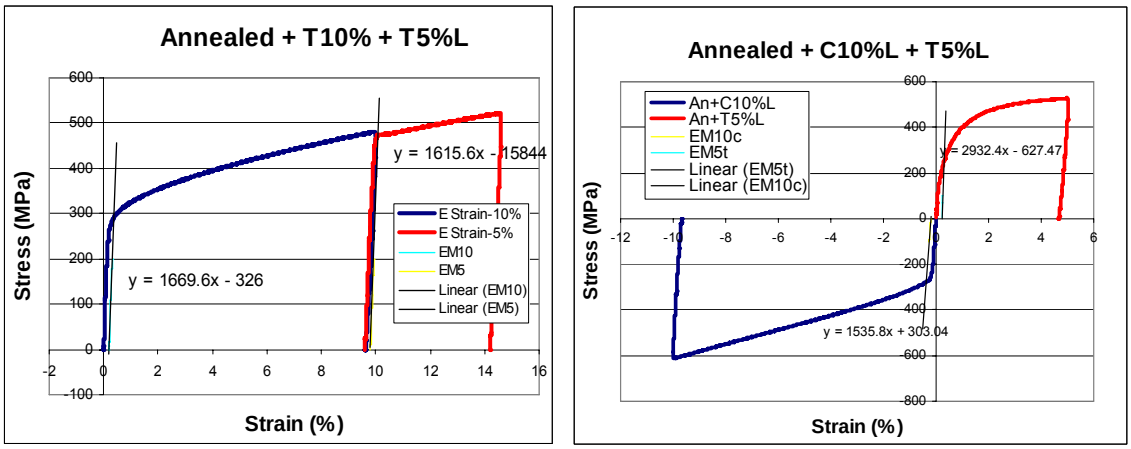

(a) (b)

Figure 32: Annealed stress-strain curves: Tension-Tension (a), Compression-Tension (b)

In contrast, in the compression-tension loading cycle, Figure 32(b), the yield strength in compression, initially around 275 MPa, was reduced to around 245 MPa after reloading in tension to 5 % strain.

(b) 5 % Initial Cold Work

The stress-strain curves for the 5 % CW are shown in Figure 33. The yield strength observed along the T-direction was slightly higher than the L-direction with values of around 375 MPa and 360 MPa respectively. The yield strength of the material along the S-direction was considerably lower, around 305 MPa.

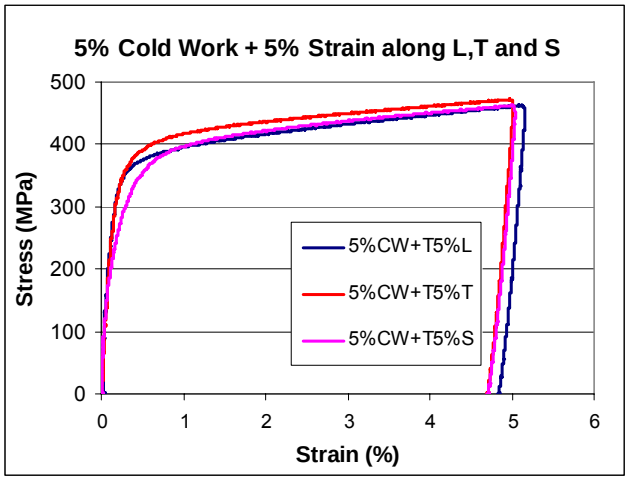

Figure 33: Stress-strain: 5% cold work + 5% subsequent tensile loading along L, T and S

(c) 10% Initial Cold Work

The stress-strain curves for 10% cold work are shown in Figure 34. Again, the L and T directions had very similar yield stresses, around 550 MPa and 545 MPa respectively. However, the yield strength in the S-direction of was significantly lower, only around 360 MPa.

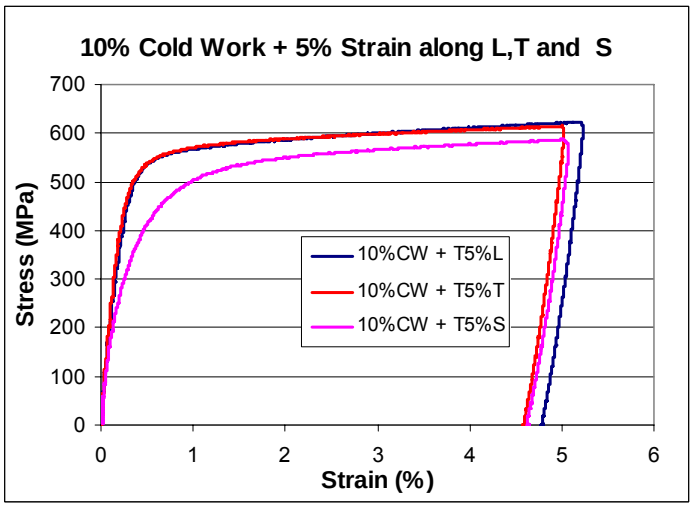

Figure 34: Stress-strain: 10% cold work + 5% subsequent tensile loading along L, T and S

(d) 20 % Initial Cold Work

The stress-strain results of 20 % CW are shown in Figure 35. The results are consistent with the 5% CW and 10% CW results. The yield strength values along the L and T-direction were around 710 MPa and 695 MPa respectively, far greater than the 450 MPa recorded along the S-

direction. However, the full plastic region could not be identified as failure occurred at the welded joint in the sample loaded along the S-direction immediately after the elasto-plastic transition region.

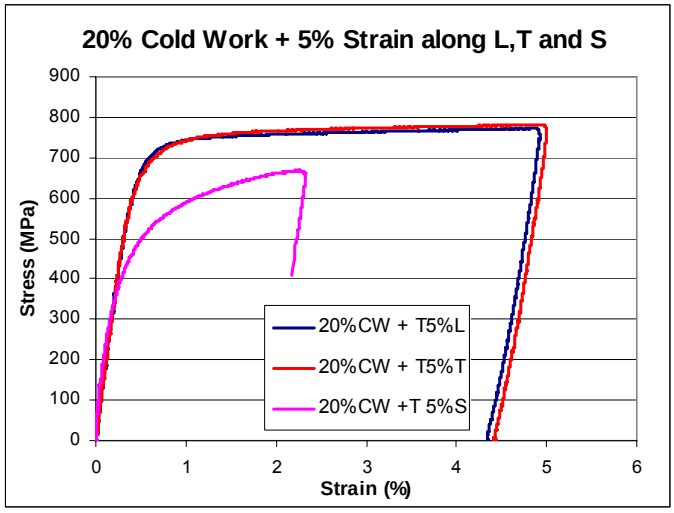

Figure 35: Stress-strain: 20% cold work + 5% subsequent tensile loading along L, T and S

(e) 40% Cold Work

The results of the stress-strain tests for 40% CW are shown in Figure 36. The 40% CW material yielded along the L and T-direction at an applied stress of around 880 MPa and 920 MPa respectively. Again the yield stress along the S-direction was considerably lower at about 655 MPa shortly before failure again occurred at the welded joint outside the specimen gauge length.

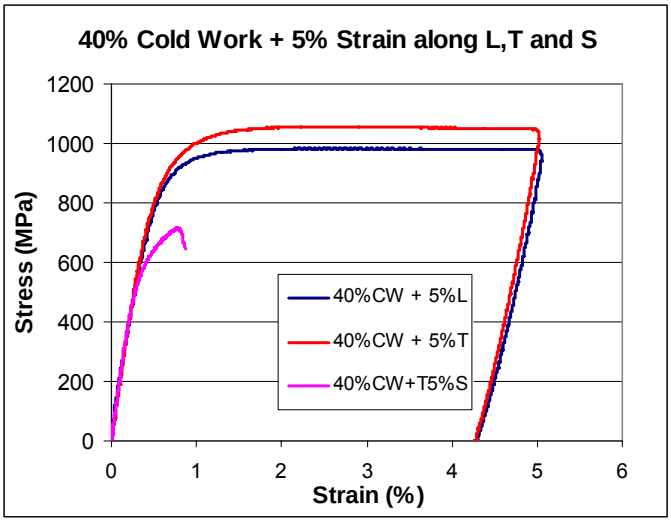

Figure 36: Stress-strain: 40% cold work + 5% subsequent tensile loading along L, T and S

Another observation from the 40% CW results was that, the ultimate tensile strength of the material tested in the T-direction is about 70 MPa greater than the L-direction. The difference is relatively higher in 40% CW than other cold work levels tested.

3.2.3.3 Neutron Diffraction Experiment

3.2.3.3.1 Residual Strain Measurement

The strain was actually measured over the angles shown in Figure 37. However, the results were restricted to the angles between the two perpendicular principal directions (specimen axis and a normal direction to it). The excluded data were mirror images of the reported ones often referred to as psi split [7]. The strain data were plotted relative to a reference point and the change in the strain value, $\Delta\varepsilon$ were evaluated from the maximum and the minimum strain values. Residual strains were measured not only in the cold work material namely 5% CW, 10% CW, 20% CW and 40% CW, but also in annealed materials *in-situ* after unloading from 10% strain in tension and in compression.

(a) Annealed

The results of the lattice elastic strain measurements on annealed materials during tension-tension and compression-tension load cycles are shown in Figures 37(a) and (b) respectively. The tensile loading to 10% strain generated tensile elastic lattice strain along the loading direction (specimen axis) and compressive elastic lattice strain perpendicular to the loading

axis. Lattice strains were investigated by considering the strongest first four diffraction peaks: 111, 200, 220 and 311 respectively. The lattice elastic responses were fairly linear and proportional in the bulk elastic region with some marginal differences toward the bulk elastic-plastic transition region, Figure 37(a) Beyond the transition region, significant deviation from the linear proportionality was observed for the 220, 111 and 200 peaks while the 311 peak shows little or no deviation. The largest increase and decrease in lattice elastic strain occurred for the 220 and 200 peaks respectively.

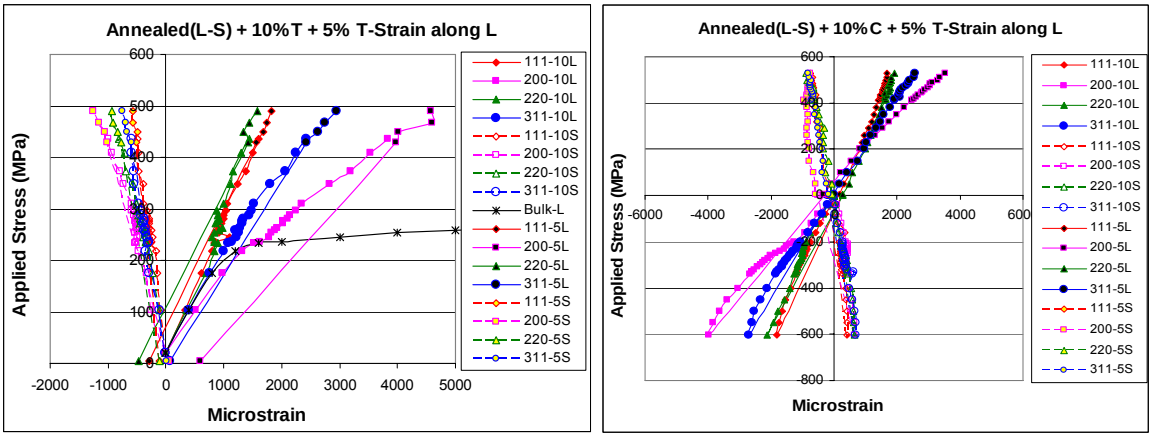

(a) (b)

Figure 37: In-situ lattice strain measurement in annealed sample initially loaded: (a) Tension-Tension (10% tensile strain, unloaded and reloaded to 5% tensile strain along L) and (b) Compression-Tension (10% in compressive strain, unloaded and reloaded to 5% tensile strain).

Residual strain measurement after unloading from the initial Tension-Tension experiment, Figure 37(a), showed that along the specimen axis, compressive residual strain remained for the 220 and 111 peaks, (-480 με and -298 με respectively). In contrast, tensile residual strain remained for the 311 and 200 peaks, with respective values of 73 με and 600 με.

The results of the Compression-Tension loading cycle are shown in Figure 37(b). The compression loading test generated residual compressive elastic lattice strains along the loading axis and tensile elastic lattice strains in the perpendicular direction. The behaviour of the diffraction peak with regards to their respective strain were quite similar to the tension-tension loading cycle except that the 111 appeared to have the greatest deviation from the linear proportionality with marginal difference to the 220 peak. On the whole, the lattice response to the applied load and during unload were consistent with the observations from the tension-tension test results (Table 4).

Generally, the anisotropy in elastic strains increased with the level of cold work in both tension-tension and compressive-tension tests. However, during the tensile reload, the anisotropy in elastic strains was more obvious in the former than the latter.

(b) 5% Cold Work

The results of the residual strain measurement in material cold worked to 5% reduction are shown in Figure 38. The change in strain, $\Delta\varepsilon$ in L-S, T-L and S-T measurement orientations were 623, 521 and 361 $\mu\varepsilon$ respectively. The results suggest that the largest change in strain occurred in L-S and the smallest difference occurred in S-T at 5% CW.

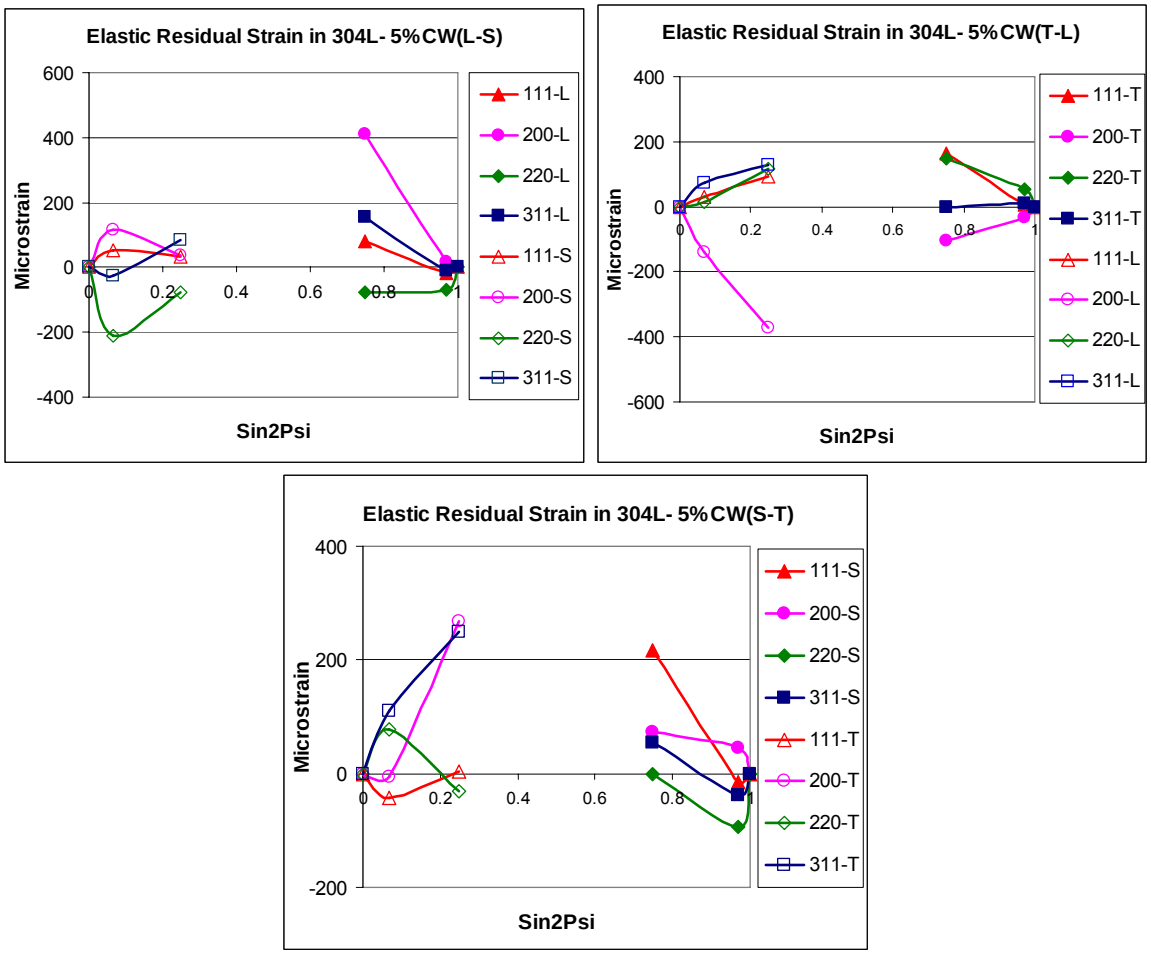

Figure 38: Residual strain measurement at 5% Cold Work (L-S, T-L and S-T)

(c) 10% Cold Work

The results of the residual strain measurement on the material cold worked to 10% CW are shown in Figure 39. The Δε for L-S, T-L and S-T measurement orientations were 733, 597 and 614 με respectively. In contrast to the 5% CW results, the largest and lowest strain difference occurred in L-S and T-L respectively.

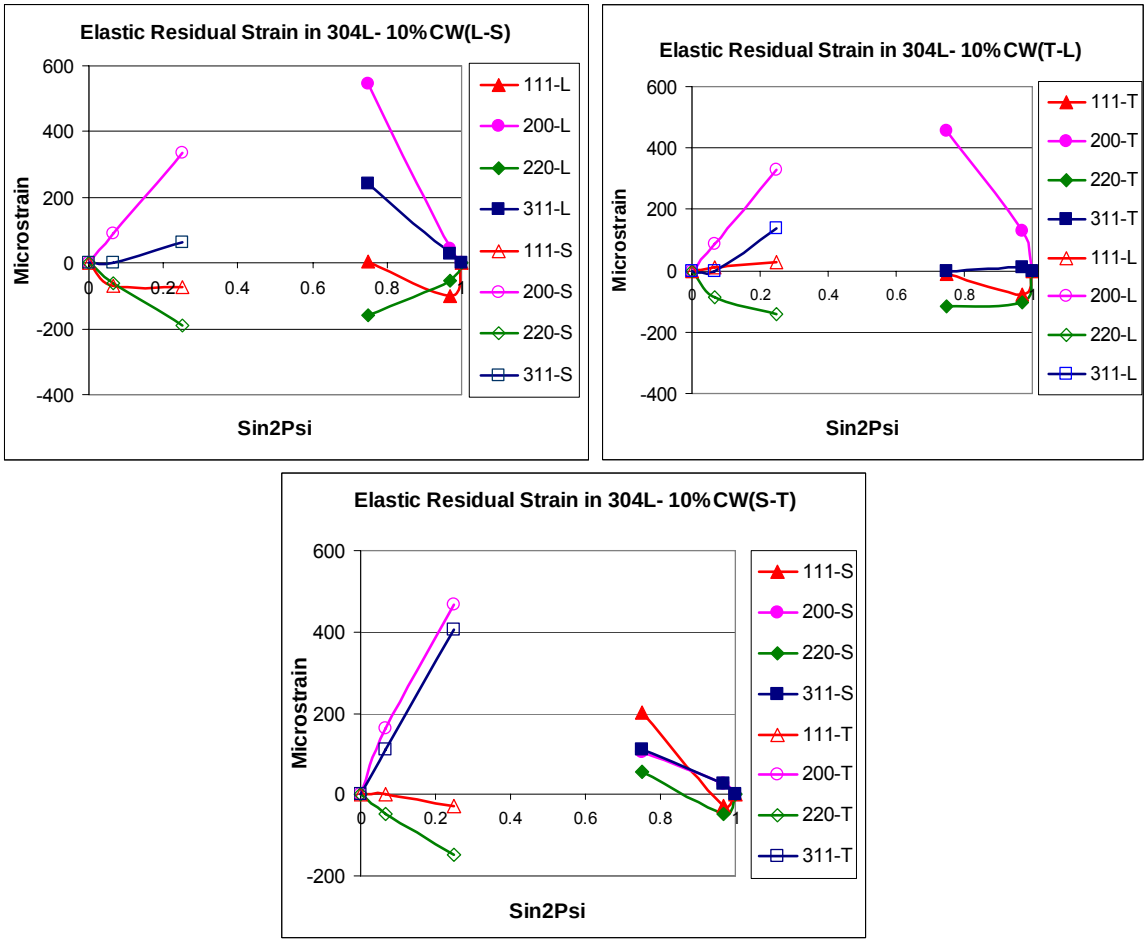

Figure 39: Residual strain measurement at 10% cold work (L-S, T-L and S-T)

(d) 20% Cold Work

The results of the residual strain measurement on 20% CW are shown in Figure 40. In line with the previous results, the L-S, T-L and S-T measurement orientation have strain difference, Δε with the values of 1009, 893 and 983 με respectively. The largest deformation occurred in L-S sample orientation while the least deformation occurred in T-L orientation.

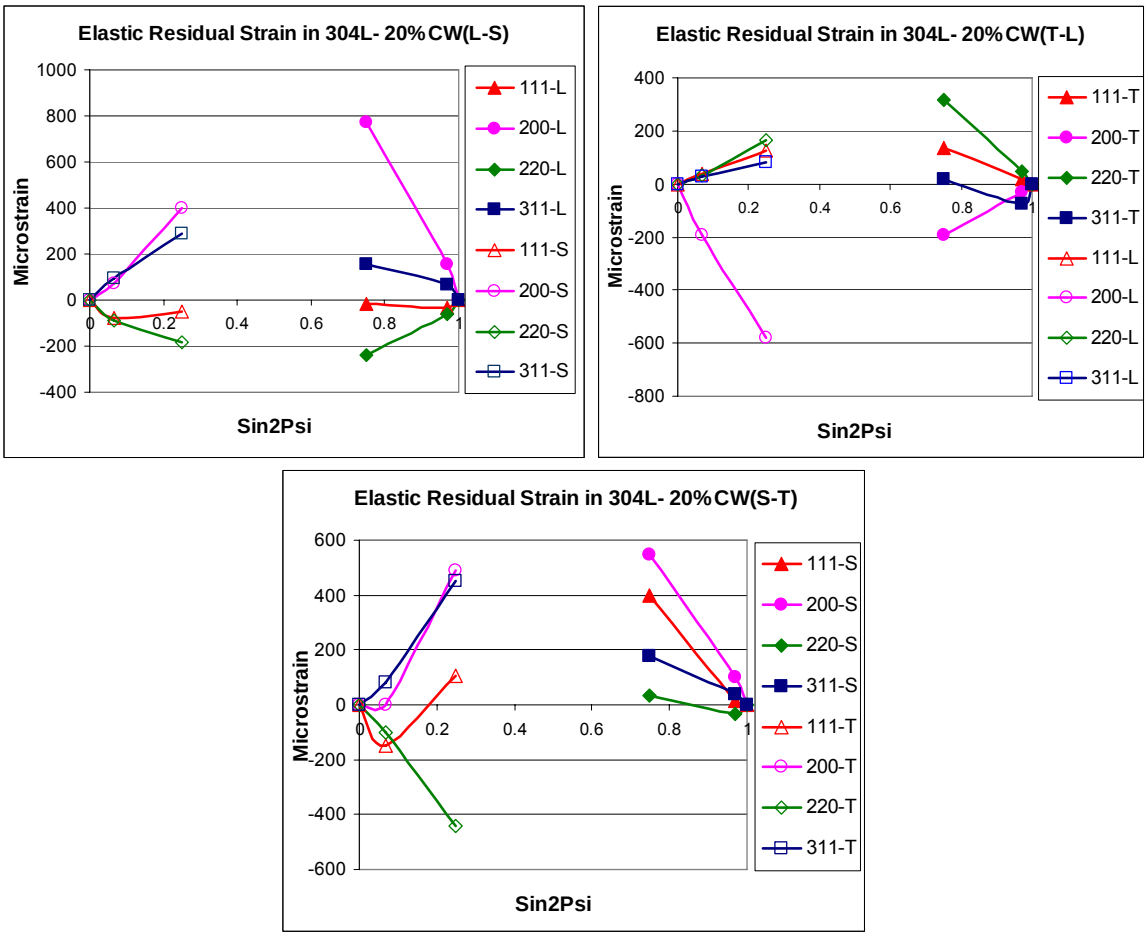

Figure 40: Residual strain measurement at 20% cold work (L-S, T-L and S-T)

(e) 40% Cold Work

The results of residual strain measurement on 40% CW material are shown in Figure 41. The strain difference, Δε in the L-S, T-L and S-T measurement orientations were 1205, 1019 and 1450 με respectively.

The summary results of the strain difference, Δε obtained from the residual strain measurement data in all the cold work materials are displayed in Table 4. Generally, the largest differences are in the L-S orientations up to the 20% CW. It is only in 40% CW where the largest differences are seen in S-T orientation whilst, the smallest differences are in the S-T orientation in 5% CW sample. Generally, the strain difference, Δε increased with the level of cold work.

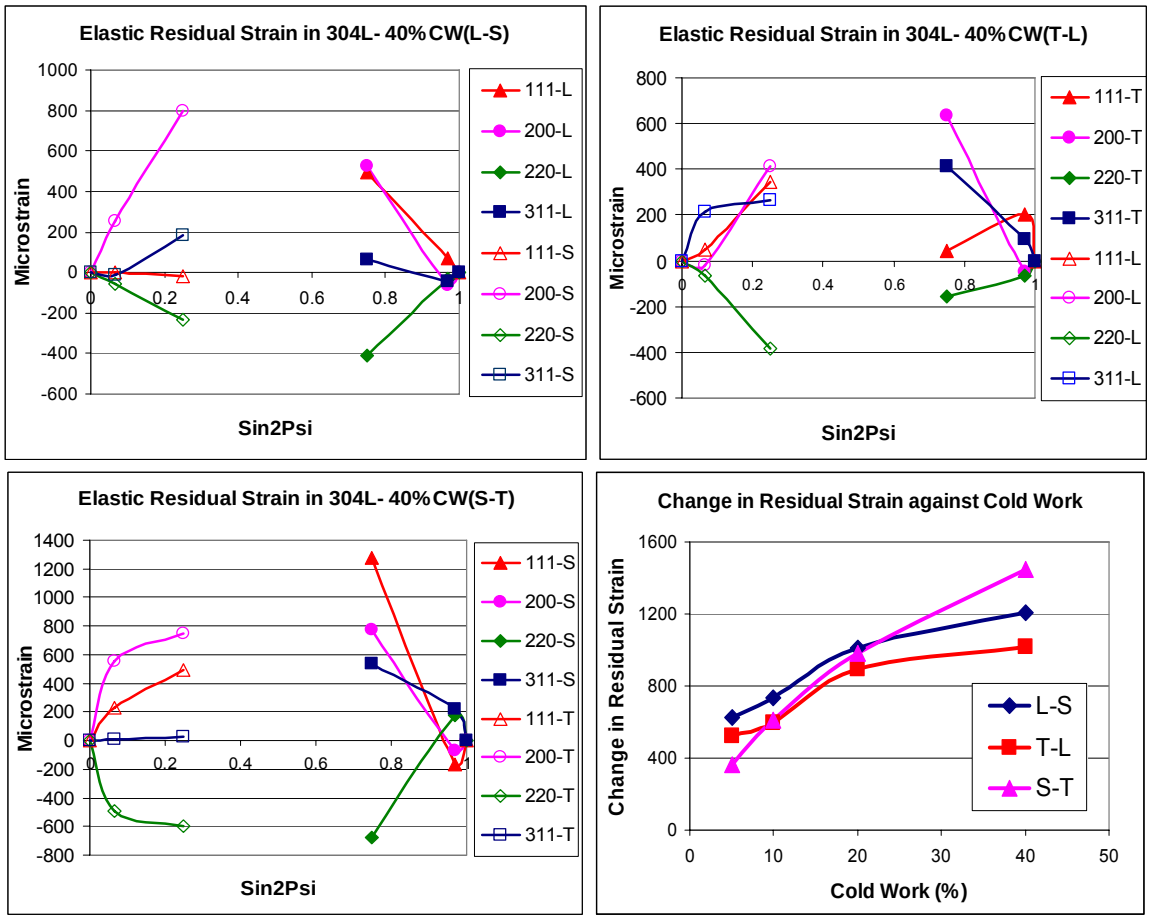

Figure 41: Residual strain measurements at 40% Cold Work (L-S, T-L and S-T) and correlation between the change in residual strain, Δε and cold work

Table 4 Summary Table of the Residual Strain Measurement

Lattice Residual Strain (με) - Specimen Axis						**Change in Residual Strain, Δε (ε_{max}-ε_{min})**				
Annealed (10% Uniaxial Strain)	**111**	**200**	**220**	**311**		**CW-Sample (Plane Strain)**	**5%**	**10%**	**20%**	**40%**
Tension-Tension	-298	600	-480	73		**L-S**	623	733	1009	1205
Compression-Tension	231	-317	275	-64		**T-L**	521	597	893	1019
						S-T	361	614	985	1450

3.2.3.3.2 *In-Situ* Loading Lattice Strain Measurement

(a) 5% Cold Work

The results of the *in-situ* loading tests carried out on material pre-strained to 5% reduction are shown in Figure 42. The material was re-strained along the 3 principal directions namely L, T and S to 5% (Figure 42). The results showed that in all cases, the peaks show different strains right from start and that the difference between them increased with the applied stress along the loading axis and normal to the loading axis. However, the lattice strain response to the applied stress for the cold rolled specimen was rather similar to the response observed for the annealed condition (Figure 37). Along the loading axis, the (220 and the 200 plane peaks have consistently remained to be the stiffest and the most compliant respectively. The largest and the lowest elastic lattice strain were observed on (200) and (220) peaks respectively (*see* Table 5). The elastic strain difference, Δε along the L, T and S direction at the maximum applied stresses were 1918, 2114 and 2602 με respectively.

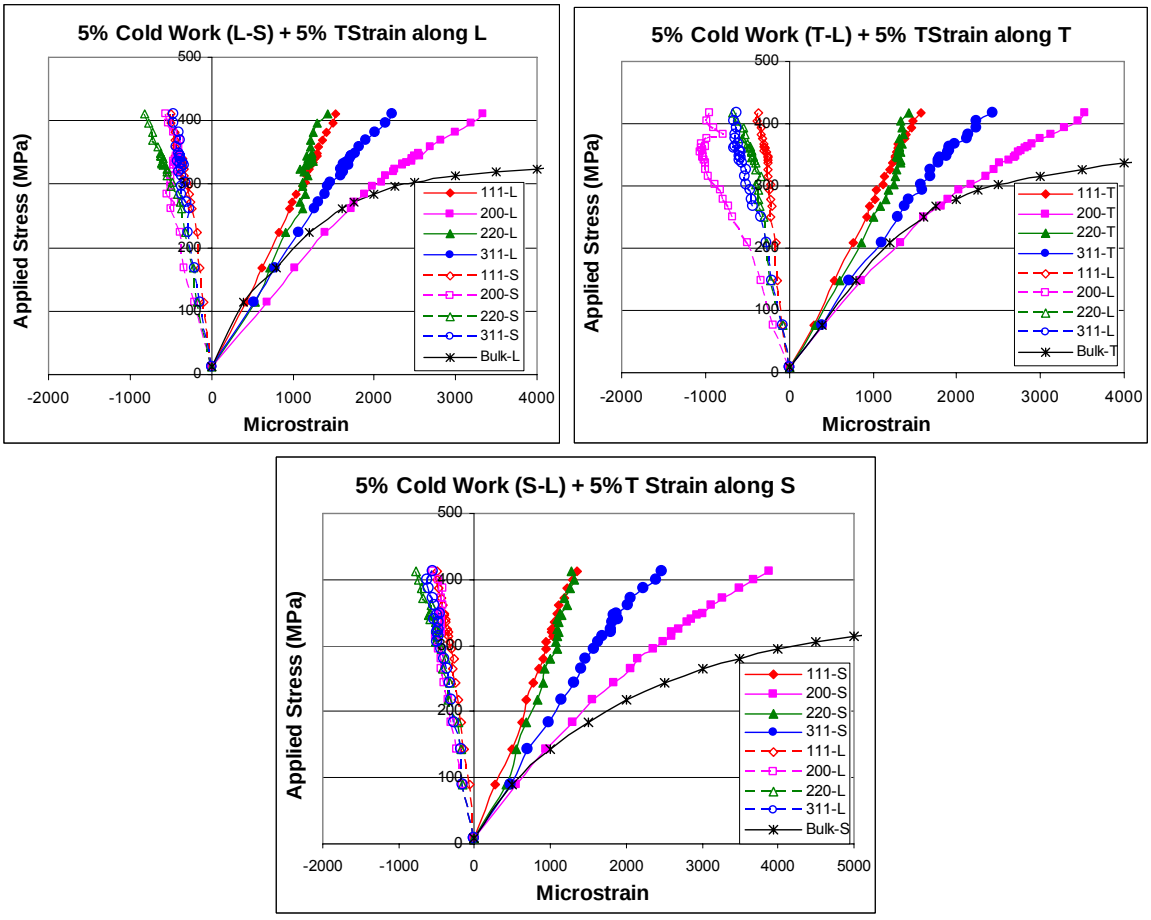

Figure 42: In-situ lattice strain measurement in 5% CW-5% tensile re-strain along L, T & S

(b) 10% Cold Work

The results of the *in-situ* loading tests carried out on the material pre-strained to 10% reduction are shown in Figure 43. The lattice strain response to the applied stress is consistent with the observation on the 5% CW results. The differences in elastic strain increase with applied stress and it is most obvious when the material was re-strained along the S-direction (Figure 43). The details of the lattice strain at the maximum applied stress during the re-strain along the principal directions are contained in Table 5. The elastic lattice strain difference, $\Delta\varepsilon$ along the L, T and S direction were 2444, 3007 and 3612 με respectively. The largest strain difference was observed when the material was re-strained along the S-direction.

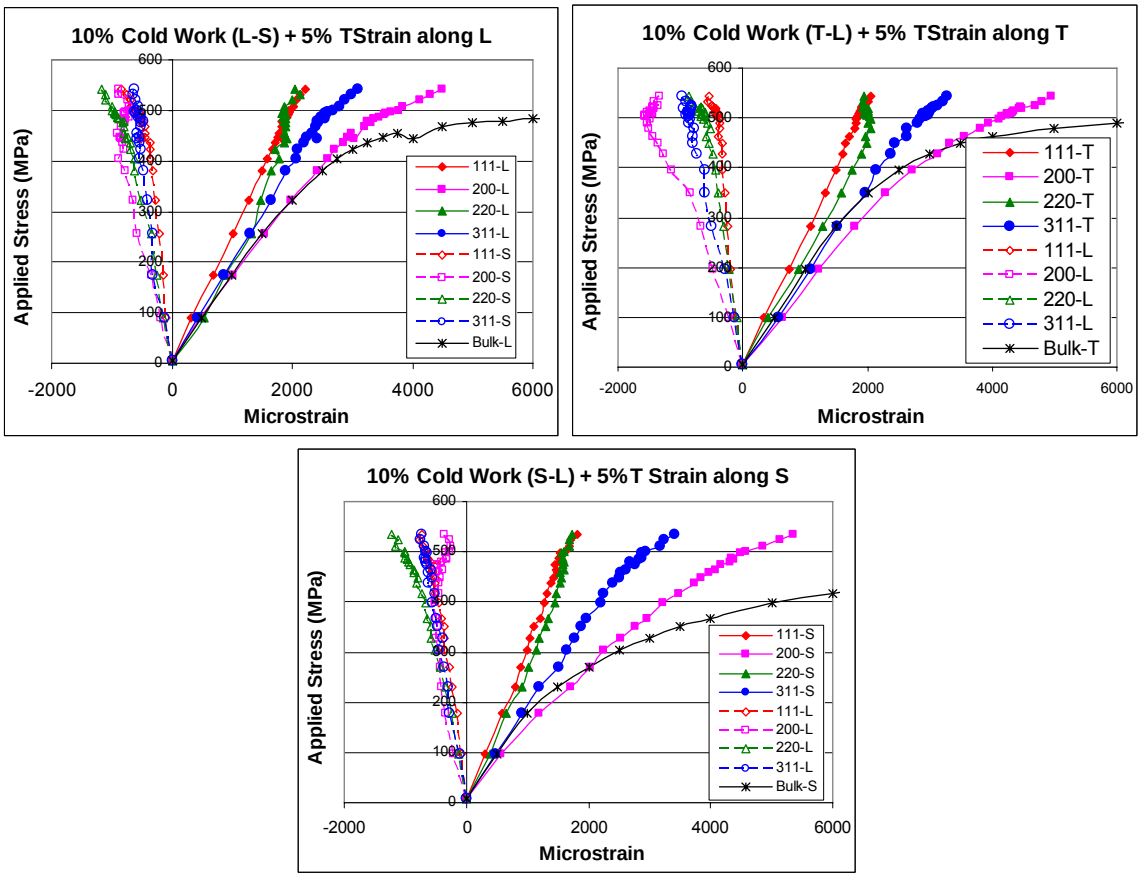

Figure 43: Lattice strain measurement in 10% CW-5% tensile re-strain along L, T & S

(c) 20% Cold Work

The results of the *in-situ* loading tests carried out on the material pre-strained to 20% reduction are shown in Figure 44. The detailed results of the elastic lattice response are contained in Table 5. The observed difference was that, the (111) peak appeared to have the

largest deviation and thus appeared to be the stiffest along the T-direction. The (111) and (220) peaks later converged with marginal difference. The test sample fabricated from the S-direction failed at the bulk strain of 3 % during the *in-situ* loading along the S-direction. The elastic lattice strain difference, Δε along the L, T and S direction were 3730, 3980 and 3997 με. The low strain difference observed along the S-direction (*see* highlighted data in Table 5) was probably caused by the sample failure. However, the largest strain difference still occurred along the S-direction. The strain data obtained during the failure was not included in the summary results shown in Figure 46 to avoid ambiguity.

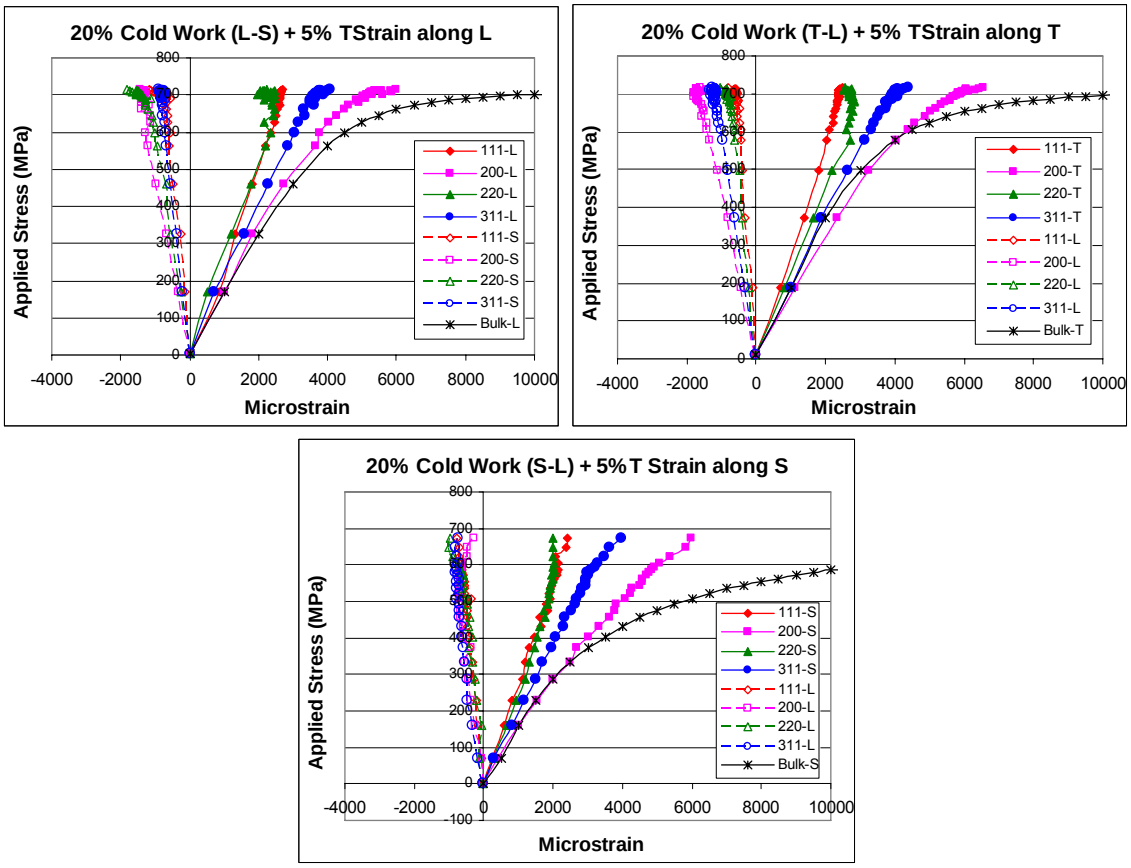

Figure 44: Lattice strain measurement in 20% CW-5% tensile re-strain along L, T & S

(d) 40% Cold Work

The results of the *in-situ* loading tests carried out on the material pre-strained to 40% reduction are shown in Figure 45. The universal grip failed during the *in-situ* loading test along the L-direction while, failure also occurred at the welded joint of the test samples for the *in-situ* loading along the S direction. The lattice strain data of the failed samples were highlighted in the Table 5. The elastic lattice strain difference, Δε along the L, T and S direction were 2689,

3458 and 2557 με respectively. Only the in-situ loading test along the T-direction was completed. The strain data obtained from the test along the S-direction was not included in the summary results shown in Figure 46 to avoid ambiguity.

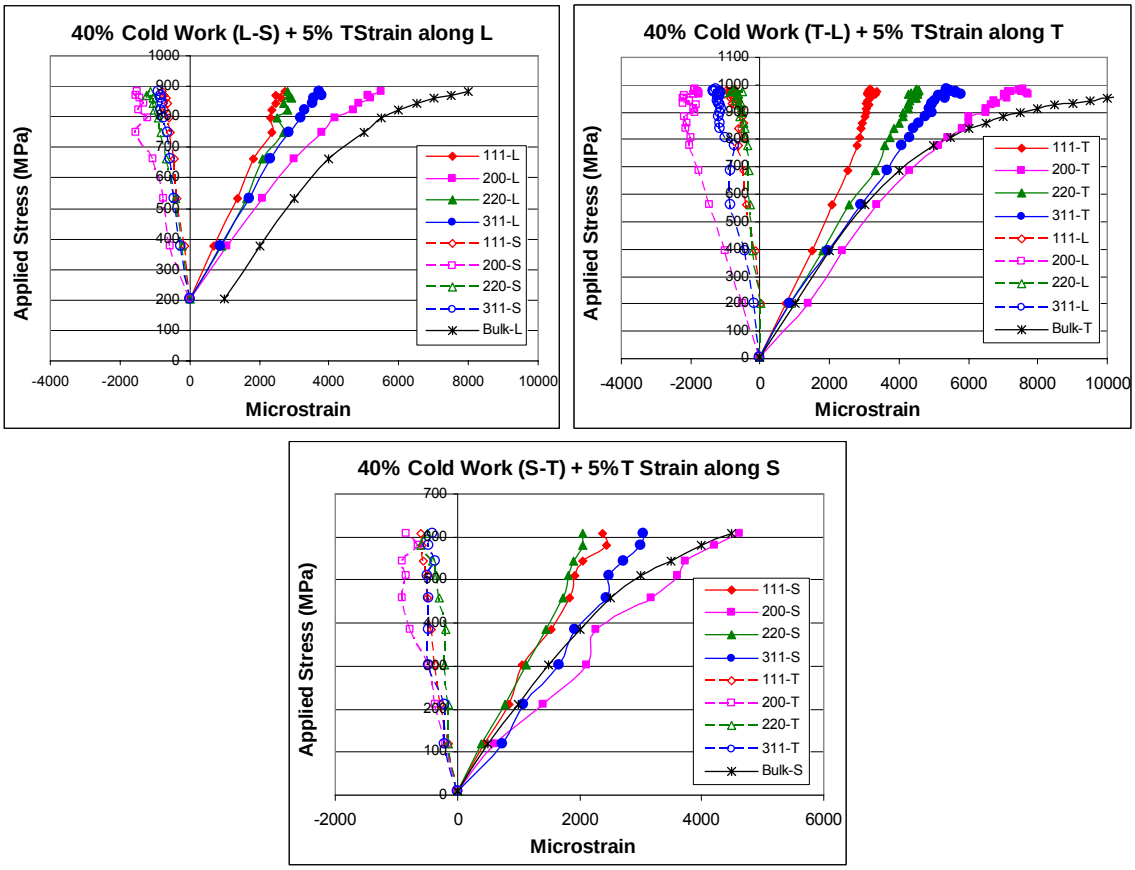

Figure 45: Lattice strain measurement in 40% CW-5% tensile re-strain along L, T & S

The correlation between the effects of pre-strain (cold work) and strain paths on the evolution of elastic lattice strain are shown in Figure 46. Generally, the elastic lattice strain difference, Δε increased with the level of pre-strain until it reaches a peak at 20% CW. The largest strain difference occurred in the material pre-strained to 20% reduction.

Table 5 Results Summary of the *In-Situ* Loading Test

CW (%)	Applied Stress	Bulk Strain	Lattice Strain (microstrain)				Δε
			111	200	220	311	$(\varepsilon_{200}-\varepsilon_{220})$
Reloading along the Longitudinal Direction							
5	410	5	1532	3343	1425	2216	1918
10	542	5	2217	4484	2040	3085	2444
20	717	5	2704	5974	2244	4064	3730
40	885	0.8	2740	5514	2824	3710	2689
Reloading along the Transverse Direction							
5	416	5	1571	3539	1425	2438	2114
10	543	5	2048	4952	1945	3279	3007
20	715	5	2501	6539	2559	4378	3980
40	966	5	3325	7734	4276	5800	3458
Reloading along the Short-Transverse Direction							
5	412	5	1359	3885	1283	2466	2602
10	533	5	1826	5344	1732	3408	3612
20	673	3	2429	5973	1976	3953	3997
40	606	0.45	2386	4619	2062	3038	2557

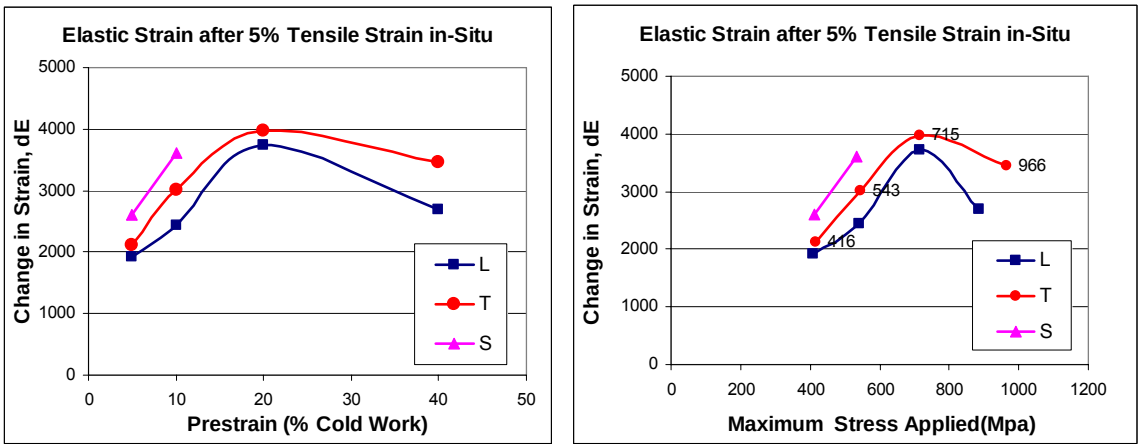

(a) (b)

Figure 46: Effect of CW and strain path on lattice strain evolution during in-situ loading: Change in strain (Δε) vs. cold work (a) and change in strain (Δε) vs. applied stress (b)

4. Discussion

4.1 Part A – Electrochemistry in acidified tetrathionate and simulated PWR environments

4.1.1 Electrochemical measurements in PWR water

Typically, the most important anodic reaction is metal dissolution, whilst the cathodic reactions are oxygen reduction and hydrogen evolution, depending on the solution pH and O_2 levels. At high temperatures, as found in light water reactors (LWRs), the concentration of dissolved oxygen largely influences the open circuit potentials, with increases to levels of ~ 80-100 ppb resulting in the oxygen reduction cathodic reaction (~-200 mV_{SHE}) dominating over the hydrogen evolution reaction (~-600 mV_{SHE}) [8-10].

The open circuit potentials generally confirmed that in aerated conditions, the PGM-doped alloys achieved a more noble (positive) potential than the standard alloy, with the ruthenium-modified alloy more effective than the palladium-doped alloy. This latter point is almost certainly due to the removal of palladium from the matrix of the alloy by formation of the PdMn intermetallic second phase particle after heat treatment, discussed in a previous report. There was little significant effect of temperature on the OCP values between 25°C and 70°C.

Deaeration by means of nitrogen gas sparging, tended to decrease the potentials of all alloys, which is the expected consequence of removal of oxygen. However, the PGM-doped alloys, particularly the Ru-containing alloy, showed evidence of increased catalytic activity for the reduction of residual oxygen (nitrogen gas sparging can only effectively remove up to 99% of the dissolved oxygen), resulting in improved passivation.

Potentiodynamic polarisation scans were obtained for pure Pt, the PGM-doped alloys and 304 SS obtained under different chemical conditions and temperatures. Both Ru and Pd additions improve the corrosion resistance, as the passive current density is lower than that for the standard alloy 304MC, although with Pd the effect is less significant than for Ru. From the slopes of the cathodic curves, it was apparent that Pt is substantially more efficient in catalysing the O_2 reduction process than Pd and Ru as well as the 304 SS,

In general, for all alloys investigated in this work, an increase in temperature from 25°C to 70°C increases the OCP of the alloy, but also increased the anodic current density. Temperature influences metal dissolution as well as diffusion of the species and reaction rates,

which in this case is the O_2 reduction rate (which increases due to faster diffusion kinetics). This effect can be rationalised in terms of the efficiency of the cathodic reaction. The noble metal additions appear to enhance the exchange current density of the oxygen reduction process, thus leading to faster passivation kinetics.

The effect of Ru concentration on the electrochemical behaviour was also investigated under aerated and deaerated conditions. The alloys investigated contained 0.11, 0.25 and 1wt. % Ru and these alloys were compared with the standard alloy. In the aerated environment, an increase in ruthenium concentration did not significantly change the anodic behaviour of the modified alloys. However, all three ruthenium alloys displayed lower passivation current densities than the standard alloy. In fact the alloys with intermediate levels of ruthenium appeared to show the best corrosion response, in terms of the passivation current density and size of the passive region. In nitrogen deaerated water, the alloy with 1 wt. % Ru showed the most noble electrochemical behaviour, presumably due to residual oxygen that was not effectively removed. In contrast to nitrogen gas sparging, deaeration with hydrogen simulates PWR conditions more effectively and enhances the reversibility of the hydrogen evolution reaction (HER):

$$\mathbf{H_2 \rightarrow 2H^+ + 2e^-}$$

It is the achievement of the lowest (i.e. most negative) possible corrosion potential that limits corrosion and mitigates against SCC in reactor conditions. This is effectively accomplished by the generation of an acceptable equilibrium for the above reaction on the metal surface and PGM alloy additions are expected to assist in achieving this equilibrium more rapidly because of their electro-catalytic activity.

In hydrogenated conditions, PGM additions lowered the electrochemical corrosion potential and increased the anodic current density of the standard alloy in the following order: Pt>Ru3MC>Pd3MC>304MC. The potential for the reversible reaction at the electrolyte pH is -0.66V vs SCE) and correspond to the measured OCP of Pt. Thus, in this environment, Pt behaved like a hydrogen electrode due to its catalytic efficiency. Similarly, it seems that Ru is more efficient than Pd for a similar PGM content (1 wt. %). Moreover, it has been demonstrated that 0.25 wt. % Ru appears to be sufficient to achieve a lower potential under hydrogenated conditions, which is important for cost considerations. Consequently, these results have shown that the addition of small amounts of Ru can lower the potential of the standard alloy under hydrogenated conditions. Previous work conducted by Kim and Andresen also showed that small amount (>0.11wt %) of Pd or Pt added to 304 SS, made the OCP

identical to that of pure Pt [11]. The catalytic effect was observed after increasing the immersion time. In PWR application this is an important aspect, since to avoid IGSCC the potential must be kept below the critical value of IGSCC initiation (-0.230V vs. SHE). The increase in anodic current density in the presence of PGM additions could be explained in terms of the high exchange current density of the hydrogen oxidation process.

The effect of Ru concentration on the electrochemical behaviour under hydrogenated conditions at 25°C was also studied. The polarisation measurements demonstrated that in alloys with ruthenium additions between 0.1 and 1 wt.%, the OCP was similar to that of pure Pt. The fact that the OCP was lower in the polarisation measurements than in the OCP measurements carried out initially, can be understood by the possible absorption of hydrogen by the materials, hence lowering the OCP.

Autoclave experiments at 260°C under high pressure and deaerated conditions demonstrated that PGM additions influenced on the electrochemical behaviour of the standard material 304SS. In these conditions, the 1% ruthenium alloy showed lower anodic dissolution that the other materials further confirming the beneficial effects of this material.

4.1.2. Electrochemical studies in acidified tetrathionate solutions

Initiation of IGC and IGSCC by potassium tetrathionate [12] or polythionic acids [13] is well known. With respect to the nuclear industry, it has been found that thiosulfate solutions (used in pressurized water reactors as an emergency quenching agent for radioactive iodine) induces IGSCC in sensitised stainless steels, possibly due to the oxidation of thiosulfate to tetrathionate by the iodine itself.

In aerated conditions, for all alloys, there was a sudden transition to more positive potentials (i.e. passivation), with the effect occurring more rapidly for the Ru alloy. This was absent in the deaerated solution suggesting that oxygen facilitates film formation. With regards to the nobility of the OCP values, the alloys followed the trend Pt>>Ru3MC>Pd3MC>304SS.

The anodic polarisation curves obtained under aerated conditions in acidified tetrathionate (pH 1.5) with a slow scan rate of 0.5 mV s^{-1} showed features around - 0.3 V_{SCE} and 0.3 V in addition to the anodic dissolution peaks and the passive region. In addition, a black sulphide film was formed on the alloy that [14] was not observed for Pt, which displayed spontaneous passivation in this environment. The film was found to more adherent on the sensitised alloys than the non-sensitised ones and was more prominent for the virgin and Pd-doped alloys than for the Ru alloys. It was concluded that that both film formation and etching occur as the result

of a cathodic reaction in the tetrathionate solution at sufficiently low pH, and that the subsequent oxidation peak at ~0.3 V_{SCE} is a feature of the film electrochemistry, or the influence of the film/etch on the electrochemistry of the underlying metal. Fang and Staehle [15] suggested possible reduction reactions as:

$$S_4O_6^{2-} + 12H^+ + 10e^- = 4S + 6H_2O$$

$$S_4O_6^{2-} + 16H^+ + 18e^- = 4HS^- + 6H_2O$$

with the latter presumably giving H_2S at sufficiently low pH (confirmed by the characteristic odour noted during these experiments). The film is likely to be the result of the reaction of one of these reaction products with the metal electrode. Tetrathionate attacks chromium depleted regions of sensitized stainless steels. The PGM additions enhance the resistance to grain boundary attack with Ru additions appearing to exhibit a more beneficial effect than Pd. No such film forms on Pt and the polarisation curve for Pt in the same solution shows no corresponding cathodic feature at ~ -0.3 V_{SCE}.

4.2 Part B – Electrochemical and mechanical studies of cold worked 304L SS

4.2.1 Electrochemical studies of CW 304 SS

The results have shown that the electrochemical properties of austenitic stainless steels are more affected by the sample orientation with respect to the rolling direction than by the level of cold work. This result is consistent with the report of Mazza *et al.* [16]. The investigation of the effect of sampe, orientation on the electrochemical behaviour of cold worked 304L SS by electrochemical measurements have consistently revealed that the nobility of OCP values followed the order S>T>L. Figure 47 shows the optical micrographs for the 5% CW-L, T & S (A-C) and 40% CW-L, T & S (D-F) obtained after the polarisation experiment.

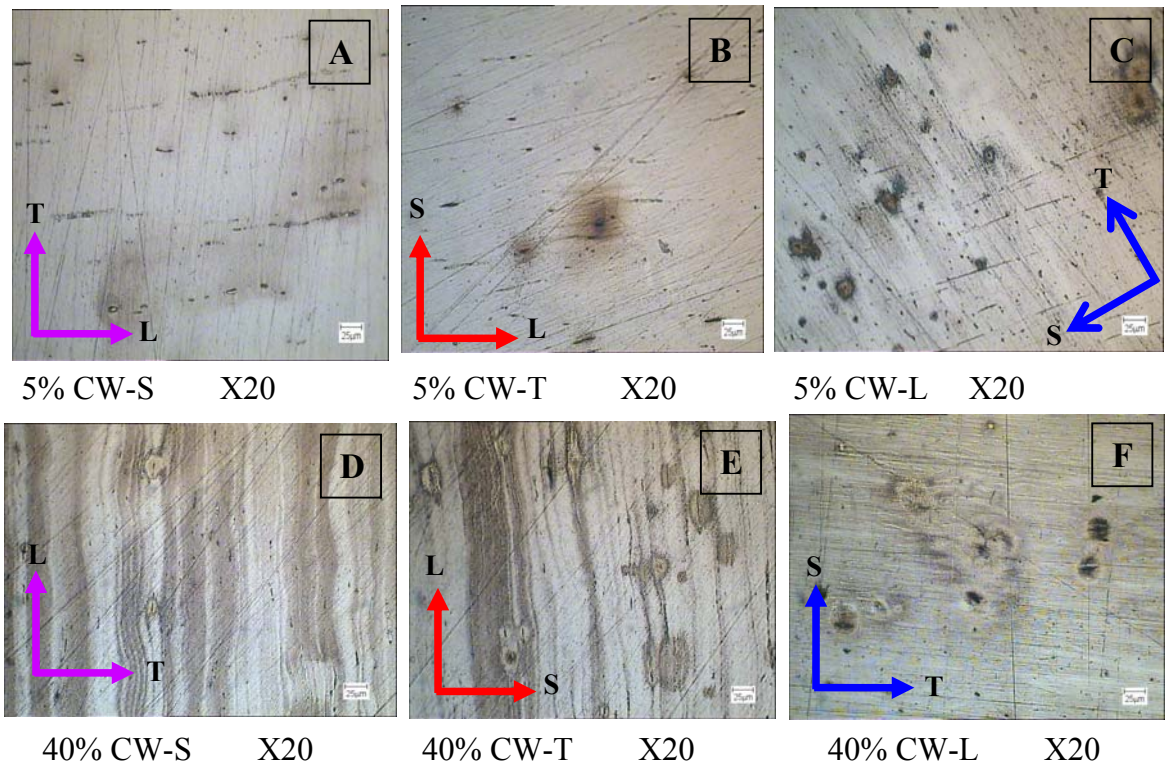

Figure 47:: Optical micrographs of 5% CW-S, T & L (A-C) and 40% CW-S, T & L (D-F) following polarisation

The reason for this is likely to relate to the grain boundary density on the respective planes. Thus, it was found that S-planes have pancake like grain structures with relatively low density of grain boundaries compared with the T-plane[17]. In contrast, the L-plane contains the highest density of grain boundaries. The report [17] has also shown that an electrochemical potential exists between the high energy grain-boundaries, which are considered to be anodic, and the grain matrix. With respect to the effect of prior cold work, the electrochemical investigations did not show any obvious and consistent trend in all three orthogonal directions.

4.2.2 Mechanical studies of 304L SS

The discussion of the results of the experiment are categorised into three sections namely: the result of hardness measurement, the results of mechanical testing and neutron diffraction test results.

4.2.2.1 Hardness Measurement

The increase in hardness value with the level of cold work is consistent with the principle work hardening during plastic deformation. Although no microscopy was performed,

the presence of strain-induced martensite (dependent on the degree of plastic deformation) may also contribute to higher hardness values of cold work materials.

4.2.2.2 Mechanical Testing

The results of the load cycle tests carried out on the annealed materials show that the yield strength of material increases when the material is reloaded in the primary strain direction as was the case in the tension-tension load cycle. The increase in yield strength during the tension-tension test is consistent with the principle of *isotropic* hardening. In contrast, the reduction in the yield strength during the compression-tension test is consistent with kinematic hardening [18, 19].

According to Orowan [20], plastic deformation leads to a dislocation pile up on barriers at internal barriers. Application of additional flow stress is thus required to overcome the resistance of the dislocations against further deformation in forward direction. However, when the loading direction is reversed, as was the case in compression-tension test, dislocation motion may occur at relatively lower flow stresses because the barriers at the rear of the dislocation are relatively less obstructive than the obstacles ahead of the dislocations [21].

The results of mechanical tests on cold worked materials suggest that the yield strength of material increases with pre-strain in all the 3 principal directions. The increase in the yield strength with the level of cold work agrees with principle of work hardening and increasing dislocation density. The effect of strain path is also obvious in all the test materials. Generally, a lower yield strength was observed in all samples re-strained along the S-direction in-line This is due to the fact that the original rolling direction was parallel to the S-direction.

4.2.2.3 Neutron Diffraction

The largest deviation from the linear proportionality during the neutron diffraction tests consistently occurred in the 200 and 220 peaks. In the residual strain measurement, the 200 and 220 planes represent the extreme conditions, and their strain data correspond to the maximum and minimum strain values from which the change in the lattice strain, $\Delta\varepsilon$ was calculated. Generally, the change in strain in all the specimen orientations increases with the level of cold work. The effect of anisotropy was also clear (e.g. Table 4) particularly between the L-S and T-L orientations, The L-S consistently showed higher strain difference than the T-L orientation. The reliability of the results of the residual strain measurement in S-T orientation may be questionable. This is because the test sample was fabricated by welding process (Figure 2) and the magnitude of the welding effects on the small size of the ASS material in the assembly is

not known. The strain data from the S-T measurement orientation should therefore be interpreted with a degree of caution. The occurrence of the largest strain difference in material re-strained along the S-direction is consistent with kinematic hardening.

5. Concluding remarks

This report provides a summary of research undertaken to understand the influence of composition and plastic strain on the electrochemistry of stainless steels doped with Platinum Group Metals, with a view to improving the physical understanding of the mechanisms of Stress Corrosion Cracking (SCC) of 304 stainless steel of the type used for a range of NNPP components.

In **Part A** of this report, the catalytic effects of the PGM metal additions to austenitic stainless steels were investigated in two different electrolytes, in order to simulate reactor water chemistry and IGSCC-inducing environments. Regarding the former system, containing boric acid and lithium hydroxide, the influence of solution temperature and dissolved oxygen concentration on both the electrochemical potential (OCP) and anodic polarisation behaviour was investigated. In this environment, Ru was shown to be significantly more effective than Pd in enhancing corrosion resistance. An increase in temperature also modifies the OCP to more noble values and increases the anodic current density. The observations were consistent with enhanced metal dissolution and diffusion of oxygen at higher temperatures.

The influence of the ruthenium concentration on electrochemical behaviour, under both aerated and deaerated conditions at 25°C, was studied and compared to 304SS. In the aerated environment, the alloy containing intermediate levels of ruthenium (*i.e.* 0.25 wt. %), displayed the most noble electrochemical behaviour. Under deaerated conditions though, the alloy with 1 wt. % ruthenium displayed the lowest anodic current density.

In hydrogenated solutions, the PGM modified alloys displayed lower OCP values and higher anodic current density than the standard alloy (*i.e*. Pt>Ru3MC>Pd3MC>304MC). This was rationalised by the fact that PGM additions increased the exchange current density for hydrogen oxidation. Interestingly, a concentration of 0.1 wt. % Ru to 304SS lowers the OCP more than 1 wt. % Ru. However, the alloy with 0.25 wt. % showed the highest anodic current density suggesting that this alloy was most effective at catalysing hydrogen oxidation.

In high-temperature electrochemical studies carried out at 260°C in an autoclave, ruthenium-doping of the 304SS alloy was beneficial in that a lower OCP was evident. In

hydrogenated water, no significant differences were noted in the anodic current densities of the three alloys.

The second electrolytic system used was the more aggressive acidified potassium tetrathionate, where dissolution and passivation phenomena were more easily resolved. For these experiments, firstly, the effect of PGM-dopants on the OCP and polarisation behaviour was studied and secondly, the influence of the scan rate on the polarisation curves was investigated. It was found that upon immersion of the alloys in aerated potassium tetrathionate solutions, an abrupt transition of the OCP to more positive potentials occurred, which was more rapid for the Ru alloy. The increase in OCP was attributed to film formation on the specimen surfaces, possibly through reaction of the products of the tetrathionate reduction with the metal surface. Analysis of the anodic polarisation curves in this environment suggests that the PGM additions enhance the corrosion resistance, again the effect most pronounced with Ru additions.

In **Part B** of the report, the conclusions on the investigation of the effect of anisotropy and level of cold reduction on the electrochemical behaviour of cold worked austenitic stainless steels can be summarised as follows:

- The effect of cold reduction on the electrochemical behaviour of austenitic stainless steels is less obvious than the effect of the specimen orientation with respect to the rolling direction.
- The short-transverse plane shows more noble electrochemical behaviour than transverse plane, while the longitudinal plane was the least noble.

The research addressing the influence of strain path on the mechanical behaviour of cold worked austenitic stainless steels has concluded that:

- The hardness value increases with the level of cold work.
- The yield strength of material increases with reloading in the forward direction whilst reloading in reverse direction lowers the yield strength of material. Generally, the yield strength of material increases with the level of cold work.
- The comparatively lower yield strength of material along the short-transverse direction than the longitudinal and transverse direction is caused by kinematic hardening.
- The largest increase and decrease in residual lattice elastic strain were observed for the 220 and 200 planes respectively. Generally, the lowest strain occurred more often in the 220 plane while the largest strain mostly occurred on 200 plane.

- The elastic anisotropy increases with the applied stress both in compression and in tension.
- The change in residual strain increases with the degree of cold work.
- Generally, the elastic lattice strain difference, $\Delta\varepsilon$ increased with the level of pre-strain.

6. References

1. Birchenall, C.E., *Physical Metallurgy*. 1959, New York: McGraw-Hill Book Company Inc.
2. Pang, J.W.L., et al., *The generation of intergranular strains on 309H stainless steel under uniaxial loading.* Acta Materialia, 2000. **48**: p. 1131.
3. Korsunsky, A.M., D.M. R., and K.E. James, *The correlation between plastic strain and anisotropy in aluminium alloy polycrystals.* Materials Science and Engineering, 2002. **A334**: p. 41.
4. Clausen, B., et al., *Lattice strain evolution during uniaxial tensile loading of stainless steel.* Materials Science and Engineering, 1999. **A259**: p. 17.
5. Woodhouse, G., et al., *Evaluation of new methods to assess mechanical aspects of material degradation, University of Manchester Materials Performance Centre Report No. MPC/R/052*. 2008.
6. *ASTM G5-94 Standard Reference Test Method for Making Potentiostatic and Potentiodynamic Anodic Polarization Measurements.* 2004.
7. Cullity, B.D., *Elements of Xray Diffraction*. 2nd ed. 1978, London: Addison-Wesley.
8. Indig, M.E., Corrosion, 1979. **35**: p. 288.
9. Macdonald, D.D., S. Smialowska, and S. Pednecker, *EPRI-NP-2853*. 1983, Ohio, Colorado: Ohio State University.
10. Andresen, P.L. and D.J. Duquette, Corrosion, 1980. **36**(8): p. 409.
11. Kim, Y.J.-. et al., *Corrosion Potential Behavior in High-Temperature Water of Noble Metal-Doped Alloy Coatings Deposited by Underwater Thermal Spraying.* Corrosion, 1996. **52**(6): p. 440.
12. Horowitz, H.H., Corros. Sci., 1983. **23**(4): p. 353.
13. Dravnieks, A. and C.H. Samans, Proceedings API, 1957. **37**: p. 100.
14. Green, S.J., *Personal Communication.* Johnson Matthey Technology, 2006.
15. Fang, Z. and R.W. Staehle, Corrosion, 1999. **55**: p. 355.
16. Mazza, B., et al., *Electrochemical and corrosion behaviour of work-hardened commercial austenitic stainless steels in acid solutions.* Corros. Sci., 1979. **19**: p. 907.
17. Ahmed, I.I., F. Scenini, and A.H. Sherry, *Metallographic characterisation of cold worked type 304 austenitic stainless steels Report No MPC/R/045.* 2007.
18. *M S&E 441#20 Lecture on Work Hardening, http://ecow.engr.wisc.edu/cgi-bin/get/msae/441/stone/notes/mse441lectureno.20kinematicvsisotropichardening.ppt, 25/03/2009*.
19. Dieter, G.E., *Mechanical Metallurgy*. 1988, London: McGraw-Hill Co.
20. Orowan, E., *Causes and effects of internal stress*, in *Internal Stress and Fatigue in Metals*. 1959, Elsevier Publishing Co.: New York.
21. Abel, A. and H. Muir, *The Bauschinger Effect and Discontinuous Yielding.* Philosophical Magazine, 1972. **26**: p. 489.